



Circumnuclear Multiphase Gas in the Circinus Galaxy. II. The Molecular and Atomic Obscuring Structures Revealed with ALMA

Takuma Izumi^{1,7} , Keiichi Wada^{2,3,4} , Ryosuke Fukushige², Sota Hamamura², and Kotaro Kohno^{5,6} 

¹National Astronomical Observatory of Japan, 2-21-1 Osawa, Mitaka, Tokyo 181-8588, Japan; takuma.izumi@nao.ac.jp

²Kagoshima University, Kagoshima 890-0065, Japan

³Research Center for Space and Cosmic Evolution, Ehime University, Matsuyama 790-8577, Japan

⁴Hokkaido University, Faculty of Science, Sapporo 060-0810, Japan

⁵Institute of Astronomy, Graduate School of Science, The University of Tokyo, 2-21-1 Osawa, Mitaka, Tokyo 181-0015, Japan

⁶Research Center for the Early Universe, Graduate School of Science, The University of Tokyo, 7-3-1 Hongo, Bunkyo, Tokyo 113-0033, Japan

Received 2018 June 18; revised 2018 August 27; accepted 2018 September 14; published 2018 October 30

Abstract

We used the Atacama Large Millimeter/Submillimeter Array (ALMA) to map the CO(3–2) and [C I](1–0) lines, as well as their underlying continuum emission, from the central ~ 200 pc region of the Circinus galaxy that hosts the nearest type 2 Seyfert-class active galactic nucleus (AGN), with a spatial resolution of ~ 6 –15 pc. The lines and continuum-emitting regions consist of a circumnuclear disk (CND; $74 \text{ pc} \times 34 \text{ pc}$) and spiral arms. The distribution of the continuum emission revealed a temperature-dependent dust geometry and possibly polar dust elongation in the torus region. The molecular mass of the CND is $M_{\text{H}_2} \sim 3 \times 10^6 M_{\odot}$, with a beam-averaged H_2 column density of $\sim 5 \times 10^{23} \text{ cm}^{-2}$ toward the AGN position, which contributes significantly to the nuclear obscuration. The [C I](1–0)/CO(3–2) ratio at the AGN position is unusually high, suggesting an X-ray-dominated region-type chemistry. We decomposed the observed velocity fields into rotational and dispersion components, and revealed a multiphase dynamic nature in the $r \lesssim 10$ pc torus region, i.e., the diffuse atomic gas is more spatially extended along the vertical direction of the disk than the dense molecular gas. Through comparisons with our model predictions based on the radiation-driven fountain scheme, we indicate that atomic outflows are the driver of the geometrical thickness of the atomic disk. This supports the validity of the radiation-driven fountain scheme in the vicinity of this AGN, which would explain the longstanding mystery of the physical origin of the AGN torus.

Key words: galaxies: active – galaxies: individual (Circinus) – galaxies: ISM – galaxies: Seyfert

1. Introduction

The unified scheme of active galactic nuclei (AGNs) postulates that the observability of a broad line region (type 1 and 2) depends on the viewing angle of an optically and geometrically thick dusty/molecular torus that surrounds the central supermassive black hole (Antonucci 1993; Urry & Padovani 1995). Spatially resolved thermal dust emission at near-infrared to mid-infrared (NIR to MIR) wavelengths in AGNs indeed support the existence of compact (< 10 pc) obscuring structures (e.g., Jaffe et al. 2004; Burtscher et al. 2013; Asmus et al. 2014).

Since the advent of the unification scheme, the physical origin of the geometrical thickness has been debated. In early theories, the torus was simplified as a continuous structure composed of dust and supported by, e.g., infrared (IR) radiation pressure and turbulence (e.g., Pier & Krolik 1992, 1993; Granato & Danese 1994; Schartmann et al. 2005). The dust distribution was later revised to be clumpy in nature (e.g., Nenkova et al. 2002, 2008a, 2008b; Höning et al. 2006; Schartmann et al. 2008; Stalevski et al. 2012), which successfully reproduced the characteristic features of the AGN spectral energy distribution (SED), including the $9.7 \mu\text{m}$ silicate feature. Replacement of the torus by a magnetocentrifugally driven disk wind containing dusty clumps was also proposed (e.g., Elitzur & Shlosman 2006; Elitzur & Ho 2009). Supported by the prevalence of circumnuclear starbursts around AGNs (e.g., Imanishi & Wada 2004; Davies et al. 2007; Esquej et al. 2014), a supernova (SN)-

driven turbulent torus model was also suggested (Wada & Norman 2002; Wada et al. 2009), where the SNe puffs up the disk gas and dust to form a toroidal structure at $\gtrsim 10$ parsec (pc) scales.

However, these models are now challenged by the existence of *polar elongation* in MIR continuum emission distributions revealed by high-resolution observations in nearby Seyfert galaxies (e.g., Tristram et al. 2014; Asmus et al. 2016; López-Gonzaga et al. 2016), which seems to contradict the donut-like dust geometry in the equatorial plane postulated in the unified scheme. Recent detailed radiative transfer simulations have revealed that a dusty hollow cone illuminated by the central engine can explain the observed morphology (Stalevski et al. 2017). Therefore, it is noteworthy that the radiation-driven fountain model (Wada 2012), in which the circulation of AGN-driven dusty outflows, failed winds, and inflows jointly form a geometrically thick structure, can naturally reproduce such a dusty hollow cone and the polar elongation at MIR wavelengths (Schartmann et al. 2014).

This fountain model, which was later complemented by the aforementioned SN feedback process and non-equilibrium X-ray-dominated region (XDR, e.g., Maloney et al. 1996) chemistry (Wada et al. 2016), predicts that the gas and dust of a \lesssim tens of parsecs scale circumnuclear disk (CND; Izumi et al. 2016) are highly dynamic and non-static, and consist of three main regions/structures that replace the classic torus: (i) low-density hot (=H II) and dusty outflows that are launched due to X-ray heating and radiation pressure at a sub-parsec region (the outflows irradiated by the central source form narrow line regions; K. Wada et al. 2018, in preparation),

⁷ NAOJ Fellow.

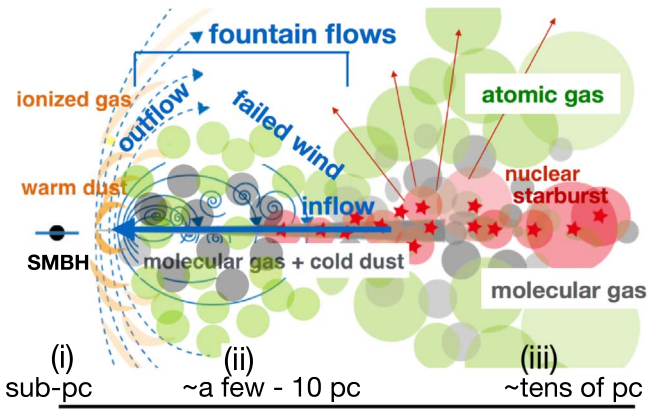


Figure 1. Schematic picture of our multiphase dynamic torus model. There are three key regions/structures: (i) low-density hot and dusty outflows at a sub-pc region, (ii) low-density cold dusty outflows and a turbulent (i.e., geometrically thick) region induced by the shocks due to failed winds from a region of a few pc to 10 pc, and (iii) a geometrically thin disk at a $\gtrsim 10$ pc region, where gas and dust can be puffed up if supernova feedback is sufficient.

(ii) low-density cold (=HI) dusty outflows and failed winds⁸ at a region of a few pc to 10 pc that cause a mid-plane disk (=HI + H₂) to become highly turbulent and then geometrically thick, and (iii) a geometrically thin disk (=HI + H₂) located at a region of $\gtrsim 10$ pc. SN-driven turbulence, if significant, can cause this latter region to become geometrically thick. This model is hereafter referred to as the *multiphase dynamic torus model* (Figure 1). The inflow gas passes through the dense mid-plane of the disk. Thus, the circulation of the inflows, outflows, and failed winds jointly form the *fountain*. Components (ii) and (iii) are basically responsible for the nuclear obscuration, with significant substructures in the column density (Wada 2015). In either region (ii) or (iii), diffuse atomic gas is spatially more extended along the vertical direction of the disk than dense molecular gas, due to complex interplay between the gas dynamics, AGN radiation, and local heating/cooling. For example, in region (ii), spatially extended outflows are preferentially observed in the atomic gas rather than molecular gas in this model. Thus, high-resolution observations of the multiphase interstellar medium (ISM) around AGNs are essential to test this picture of the multiphase gas circulation.

The Atacama Large Millimeter/submillimeter Array (ALMA) has the capability to perform such observations. Indeed, it has finally begun to detect cold molecular gas and dust emission from the central $\lesssim 10$ pc region of nearby AGNs, including NGC 1068 (Gallimore et al. 2016; García-Burillo et al. 2016; Imanishi et al. 2016, 2018), NGC 1377 (Aalto et al. 2017), Centaurus A (Espada et al. 2017), NGC 1097 (Izumi et al. 2017), and NGC 5643 (Alonso-Herrero et al. 2018). However, as these studies observed dense molecular gas only, the physical and chemical nature of multiphase gas remain unclear. This situation could be improved by using the atomic carbon line [C I](³P₁ – ³P₀) \equiv [C I](1–0) that is now observable with ALMA Band 8 for the case of nearby galaxies (Krips et al. 2016; Miyamoto et al. 2018). Contrary to the prediction of classic chemical models that C I is distributed in a thin layer between the ionized part and the shielded molecular part of a cloud (e.g., Hollenbach & Tielens 1999), it is now well known that C I is actually concurrent through the cloud (e.g., Ojha et al. 2001; Ikeda et al. 2002; Shimajiri et al. 2013). This is likely

⁸ A part of the outflow that falls back to the disk due to disk and SMBH gravities.

due to the different formation timescale between C I and CO (Suzuki et al. 1992), and/or strong interstellar turbulence (Glover et al. 2015). It is noteworthy that in active environments with strong radiation fields, such as an XDR (e.g., Maloney et al. 1996), C-bearing species such as CO are dissociated and enhance the abundance of C I. Thus, C I lines will be excellent probes of AGN signatures.

In this work, we present our high-resolution ($< 1''$) ALMA Cycle 4 observations of the CO(3–2) ($\nu_{\text{rest}} = 345.7960$ GHz) and the [C I](1–0) ($\nu_{\text{rest}} = 492.1607$ GHz), as well as the underlying continuum emission toward the central ~ 200 pc region of the Circinus galaxy (hereafter, denoted as Circinus). Our aim is to investigate the nature of the circumnuclear obscuring material by focusing particularly on the differences in the dynamical or geometrical structures as a function of the phase of the gas (molecular versus atomic). The observed properties will be compared to our multiphase dynamic torus model, where key parameters (e.g., black hole mass, Eddington ratio, gas mass) were matched to those measured in Circinus, as well as post-processed non-local thermodynamic equilibrium (non-LTE) radiative transfer calculations were performed for multiple CO lines (our Paper-1, Wada et al. 2018) and C I lines (this work).

1.1. Our Target: The Circinus Galaxy

Circinus is a spiral galaxy (SAB; de Vaucouleurs et al. 1991) with a high inclination angle on the galactic scale ($\sim 65^\circ$; Freeman et al. 1977), and hosts the nearest ($D = 4.2$ Mpc, $1'' = 20.4$ pc; Tully et al. 2009) type 2 Seyfert nucleus (Oliva et al. 1994; Moorwood et al. 1996). It shows a one-sided ionization cone and outflowing gas that extends up to kiloparsec scales in H α , [O III], and several other coronal emission lines (e.g., Marconi et al. 1994; Veilleux & Bland-Hawthorn 1997; Müller Sánchez et al. 2006). The genuine existence of an obscured type 1 nucleus was confirmed by the spectropolarimetric detection of a broad H α line (~ 3300 km s⁻¹; Oliva et al. 1998). Circinus is also undergoing modest star-forming activity, as measured using far-infrared luminosity (star formation rate (SFR) \sim a few M_\odot yr⁻¹; Moorwood & Glass 1984; Elmouttie et al. 1998b) and several hydrogen recombination lines (e.g., Marconi et al. 1994; Wilson et al. 2000), while the $\lesssim 100$ pc scale SFR is admittedly low ($\sim 0.1 M_\odot$ yr⁻¹; Esquej et al. 2014); thus, significant SN feedback might not be expected there.

As is typical in the case of a late-type galaxy, a huge amount of molecular gas ($\gtrsim 10^{8-9} M_\odot$) was detected in Circinus through observations of multi- J CO lines including isotopologues, as well as other dense gas tracers such as HCN and HCO⁺ (e.g., Aalto et al. 1991; Israel 1992; Curran et al. 1998; Elmouttie et al. 1998b; Curran et al. 1999, 2001, 2008; Hitschfeld et al. 2008; Zhang et al. 2014; Israel et al. 2015). While the intense HI emission is distributed in a ~ 10 kpc radius region dominated by large-scale spiral arms (Jones et al. 1999), molecular gas is concentrated in the inner ~ 1 kpc radius region (Curran et al. 1998, 2008; Elmouttie et al. 1998b). An expected morphology for that molecular gas structure, with the H₂ mass (M_{H_2})⁹ of $\sim 4 \times 10^8 M_\odot$ ($r < 440$ pc; Elmouttie et al. 1998b), has been a ring/disk-like one plus widespread outflows perpendicular to the morphological major axis of this galaxy

⁹ The standard Galactic CO-to-H₂ conversion factor of $\sim 2 \times 10^{20}$ cm⁻² (K km s⁻¹)⁻¹ is assumed for most of the previous M_{H_2} measurement, although Zhang et al. (2014) suggested a factor of ~ 5 lower value in Circinus through the physical modeling of multi- J CO emission lines.

Table 1
Log of Our ALMA Observations

Line	Date (UT)	Number of Antennae	Baseline (m)	On-source time (minutes)	Calibrator			T_{sys} (K)
					Band pass	Gain	Flux	
CO(3–2)	2016 Nov 24	42	15–704	42.5	J1427-4206	J1424-6807	J1427-4206	~130
	2016 Nov 26	42	17–704	42.5	J1427-4206	J1424-6807	J1617-5848	~140
	2017 May 5	47	15–1124	42.5	J1427-4206	J1424-6807	J1427-4206	~140
[C I](1–0)	2017 Mar 18	43	15–287	31.5	J1427-4206	J1424-6807	J1427-4206	~500

Table 2
Achieved Cube Parameters

Emission	ν_{rest} (GHz)	Beam (" × ") (°)	Beam (pc × pc)	rms (mJy beam ⁻¹)	Peak (mJy beam ⁻¹)
CO(3–2)	345.796	0.29 × 0.24 (153.6)	5.9 × 4.9	0.37	301
Band 7 continuum	351	0.29 × 0.24 (156.0)	5.9 × 4.9	0.08	22.4
[C I](1–0)	492.161	0.71 × 0.66 (95.9)	14.5 × 13.4	3.10	1435
Band 8 continuum	485	0.71 × 0.65 (94.2)	14.5 × 13.2	0.80	87.8

Note. In the line cubes, rms sensitivities indicate the values at a velocity resolution of 10 km s⁻¹.

(Curran et al. 1998, 1999). However, recent $\sim 2''$ – $3''$ resolution CO(1–0) mapping with ALMA imaged instead a more spiral arm-like gas distribution (Zschaechner et al. 2016), while revealing another molecular outflow at $35''$ northwest of the nucleus.

With regard to the nuclear scale, X-ray spectra below 10 keV exhibit flat continuum and prominent 6.4 keV Fe K α line emission, indicative of strong Compton scattering (Matt et al. 1996). Subsequent harder X-ray observations at >30 keV confirmed the existence of the Compton-thick nucleus (e.g., Guainazzi et al. 1999; Matt et al. 1999), with a line-of-sight obscuring column density of $N_{\text{H}} = (6 - 10) \times 10^{24}$ cm⁻², and an absorption-corrected 2–10 keV intrinsic luminosity of $L_{2-10\text{keV}} = (2.3\text{--}5.1) \times 10^{42}$ erg s⁻¹, respectively (Arévalo et al. 2014). Detections of H₂O mega-masers at both millimeter and submillimeter wavelengths at the heart of Circinus support the idea that a dense Keplerian disk is located there (Greenhill et al. 1997, 2003; Hagiwara et al. 2013), with the mass of the central supermassive black hole (SMBH) given as $M_{\text{BH}} = (1.7 \pm 0.3) \times 10^6 M_{\odot}$ (Greenhill et al. 2003). With this M_{BH} , Tristram et al. (2007) estimated the Eddington ratio of the AGN as ~ 0.2 .

Our prime reason for studying Circinus is that it clearly exhibits parsec-scale polar elongation at MIR continuum emission (Tristram et al. 2014), which makes it an ideal laboratory to test our multiphase dynamic torus model. We describe the ALMA Cycle 4 observations in Section 2. The continuum emission maps are shown in Section 3, while line emission distributions and their ratio are reported in Section 4. Details of the gas kinematics of both the CO(3–2) and the [C I](1–0) lines are presented in Section 5. We compare the observed torus properties with the predictions of our multiphase dynamic torus model in Section 6. Finally, our conclusions are summarized in Section 7.

2. Observations and Data Analysis

2.1. ALMA Observations

We observed Circinus with ALMA Band 7 and 8 during 2016–2017 using 42–47 antennas, as a Cycle 4 program

(ID = 2016.1.01613.S, PI = T. Izumi). Table 1 summarizes the log of our observations. Observations were conducted in a single pointing with fields of view of $18''$ (Band 7) and $13''$ (Band 8), which fully covered the central $\sim 2''$ of the CND (see Section 4). The expected maximum recoverable scales per pointing are $\sim 7''$ (Band 7) and $\sim 5''$ (Band 8). We set the phase tracking center to $(\alpha_{\text{J2000.0}}, \delta_{\text{J2000.0}}) = (14^{\text{h}}13^{\text{m}}09^{\text{s}}950, -65^{\circ}20'21''.0)$, which is one of the nuclear 22 GHz H₂O maser spots of Circinus (Greenhill et al. 2003). The angular separations between this tracking center and the phase calibrators are $\sim 3''$. In both Band 7 and 8 observations, one of the four spectral windows (each with a width of 1.875 GHz) was used to fully cover the CO(3–2) or [C I](1–0) emission lines, both in the 2SB dual-polarization mode.

Data reduction, calibration, and analyses were performed with CASA version 4.7 (McMullin et al. 2007) in the usual way. The line and underlying continuum emission were reconstructed using the CLEAN task with Briggs weighting (robust = 0.5). The velocity spacings of the original data were 3.4 km s⁻¹ (Band 7) and 2.4 km s⁻¹ (Band 8) per channel, but several channels were binned to improve the signal-to-noise ratio, which resulted in a final and common velocity resolution of ~ 10 km s⁻¹. Note that velocities are expressed in the optical convention in this work (local standard of rest [LSR] frame).

The achieved synthesized beams and rms sensitivities are listed in Table 2. The rms values in the line cubes were measured at channels free of line emission (i.e., thermal noise), whereas those of the continuum maps were measured in areas free of such emission. These continuum emission were subtracted in the uv plane before making the line cubes. Throughout this paper, the pixel scale of Band 7 maps is set to $0''.03$, whereas that of Band 8 maps is $0''.1$, and emission with $<1.5\sigma$ are clipped to enhance the clarity of the images. The kinematic position angle (PA) of the major axis is defined to be on the receding half of the galaxy, taken anti-clockwise from the north direction on the sky. Given this definition, we added 180° to some morphological PAs reported in previous works to maintain consistency. The absolute flux uncertainty is $\sim 10\%$ according to the ALMA Cycle 4 Proposer’s Guide, but the

displayed errors indicate only statistical ones unless otherwise mentioned. Some parts of our analyses were also performed with the MIRIAD package (Sault et al. 1995).

2.2. Ancillary Data

We retrieved the *Hubble Space Telescope* (*HST*) Planetary Camera images (PC-F656N, F606W, F814W) of Circinus from the Hubble Legacy Archive.¹⁰ The images were calibrated using the *HST* pipeline. Continuum emission was subtracted from the F656N image using the adjacent continuum following standard line extraction procedures to construct an image of the H α emission line. The structures seen in the resultant image are consistent with those found in previous works (e.g., Marconi et al. 1994; Wilson et al. 2000). We also use the *Ks*-band image obtained with the NaCo/VLT (Mezcua et al. 2016) to compare the spatial distributions of the continuum emission.

3. Continuum Emission

3.1. Spatial Distributions

Figure 2 shows the spatial distributions of the ALMA Band 7 ($\nu_{\text{rest}} = 351$ GHz or $\lambda_{\text{rest}} = 854$ μm) and 8 ($\nu_{\text{rest}} = 485$ GHz or $\lambda_{\text{rest}} = 618$ μm) continuum emission at the central $10'' \times 10''$ (~ 200 pc \times 200 pc) and $2'' \times 2''$ (~ 40 pc \times 40 pc) regions of Circinus. The total fluxes are ~ 66.5 mJy (Band 7) and ~ 320 mJy (Band 8) within the $10''$ box. Each of the emission peaks at $\alpha_{\text{ICRS}} = 14^{\text{h}}13^{\text{m}}09^{\text{s}}.948$, and $\delta_{\text{ICRS}} = -65^{\circ}20'21''.05$, which coincides with the AGN position identified by the very long baseline interferometry (VLBI) H $_2$ O maser observations ($\alpha_{\text{J2000.0}} = 14^{\text{h}}13^{\text{m}}09^{\text{s}}.953$, $\delta_{\text{J2000.0}} = -65^{\circ}20'21''.187$; Greenhill et al. 2003) within positional uncertainties. Hereafter, we define our continuum peak position as the AGN location. The peak flux densities are 22.4 mJy beam $^{-1}$ (Band 7) and 87.8 mJy beam $^{-1}$ (Band 8), respectively.

Although the achieved angular resolutions were admittedly different (Table 2), consistent spatial distributions can be identified between the Band 7 and 8 maps. The continuum-emitting regions appear to consist of (likely) three spiral arms which converge to the central bright CND or jointly constitute the CND: these structures are better echoed by the CO(3–2) and [C I](1–0) spatial distribution maps (see also Figure 6 as a reference). Note that we were unable to find a clear indication of the nuclear gaseous bar postulated by Maiolino et al. (2000) southeast, nor an expected counter bar northwest, of the nucleus. This may imply that an aligned configuration of dense molecular clouds in the spiral arms (Section 4), viewed with a high inclination, might have been mistaken as a bar.

3.2. Physical Nature of the Continuum Emission

The nature of the observed submillimeter continuum emission is of interest because the obscuring structure of this AGN would begin to be directly traced at the high resolutions obtained here. Although this galaxy possesses a radio jet (Harnett et al. 1990; Elmouttie et al. 1998a; Murphy et al. 2010), we first argue that contamination by such synchrotron emission is not significant at the ALMA Band 7 and 8 frequencies. For example, a Band 7 flux density at the central $1''.4$ region expected by extrapolating the $\lambda = 6$ cm emission (50 mJy) with a typical synchrotron spectral index¹¹ of $\alpha = -0.7$ is only ~ 2.5 mJy, which is ~ 9

times smaller than the value measured at a much smaller beam ($0''.29 \times 0''.24$) placed at the AGN position. Note that Elmouttie et al. (1998a) revealed a very flat radio spectral index at the nuclear region of Circinus at $\nu_{\text{rest}} \lesssim 8$ GHz primarily due to the optically thick nature at that frequency range. However, it is more reasonable to adopt the above $\alpha = -0.7$ for higher frequencies, where synchrotron emission becomes optically thinner.

A Band 8 to 7 flux density ratio at the AGN position, after matching the Band 7 *uv* range and beam size to the Band 8 ones (*uv* range $\simeq 25$ –470 k λ ; the resultant Band 7 flux density = 26.3 mJy beam $^{-1}$), revealed a steep spectral index of 3.72, or dust emissivity index¹² of $\beta = 1.72$. This is consistent with a typical β index observed in local star-forming galaxies (~ 1.8 ; Clemens et al. 2013). Thus, the nuclear submillimeter SED of Circinus is dominated by thermal dust emission. We found that the Band 8 continuum flux density at the AGN position is almost consistent with the value expected by the $T_{\text{dust}} \sim 300$ K blackbody model in Tristram et al. (2014), which was introduced to describe the observed IR SED at the (circum)nuclear region. Meanwhile, the Band 7 flux density at the same position falls by a factor of a few below the model prediction, which seems to reflect the fact that the dust continuum emission tends to follow the modified blackbody spectrum more, rather than the blackbody model, at a longer wavelength.

3.3. Relative Locations

It is remarkable that the extended spiral arm-like or filamentary structure seen around the CND in our submillimeter continuum maps traces the region that is radially farther from the center than the nuclear bright V-shaped structure seen in the *Ks*/F814 flux ratio map (Figure 3: the latter seems to collimate the ionized cone seen in the H α line emission distribution) that enhances the distribution of warm dust emission (Mezcua et al. 2016). This indicates the existence of temperature-dependent dusty structures around this AGN. This relative geometry, viewed with a high inclination angle ($\sim 65^{\circ}$ – 75° , Freeman et al. 1977; Elmouttie et al. 1998b; Tristram et al. 2014), is also consistent with the prediction of our multiphase dynamic torus model where the warm dust is embedded in outflows at the inner part of the disk, and the cold dust is located in the extended disk (Schartmann et al. 2014; Wada et al. 2016, see also Figure 1). Within the framework of our model, the nuclear warm dust seen in the *Ks*/F814 ratio map is thus considered to be distributed in a geometrically thick volume, whereas the cold dust is in a thinner structure. This warm dust carries only $\sim 1/3$ of the obscuring matter required to make a type 1 Seyfert nucleus appear as an obscured type 2 nucleus such as Circinus (Mezcua et al. 2016). Thus, an additional absorber is required to completely obscure the nucleus: we suggest that the extended cold material in the CND studied here contributes to that obscuration (see also Section 4).¹³

¹² Flux (thermal dust) $\propto \nu^{2+\beta}$.

¹³ We do not estimate dust mass here based on our continuum measurements because the temperature T_{dust} of the extended cold dust component, which would be a spatially different structure from the warm dust component (~ 300 K blackbody), is unknown at present.

¹⁰ <https://hla.stsci.edu>

¹¹ Flux (synchrotron) $\propto \nu^{\alpha}$.

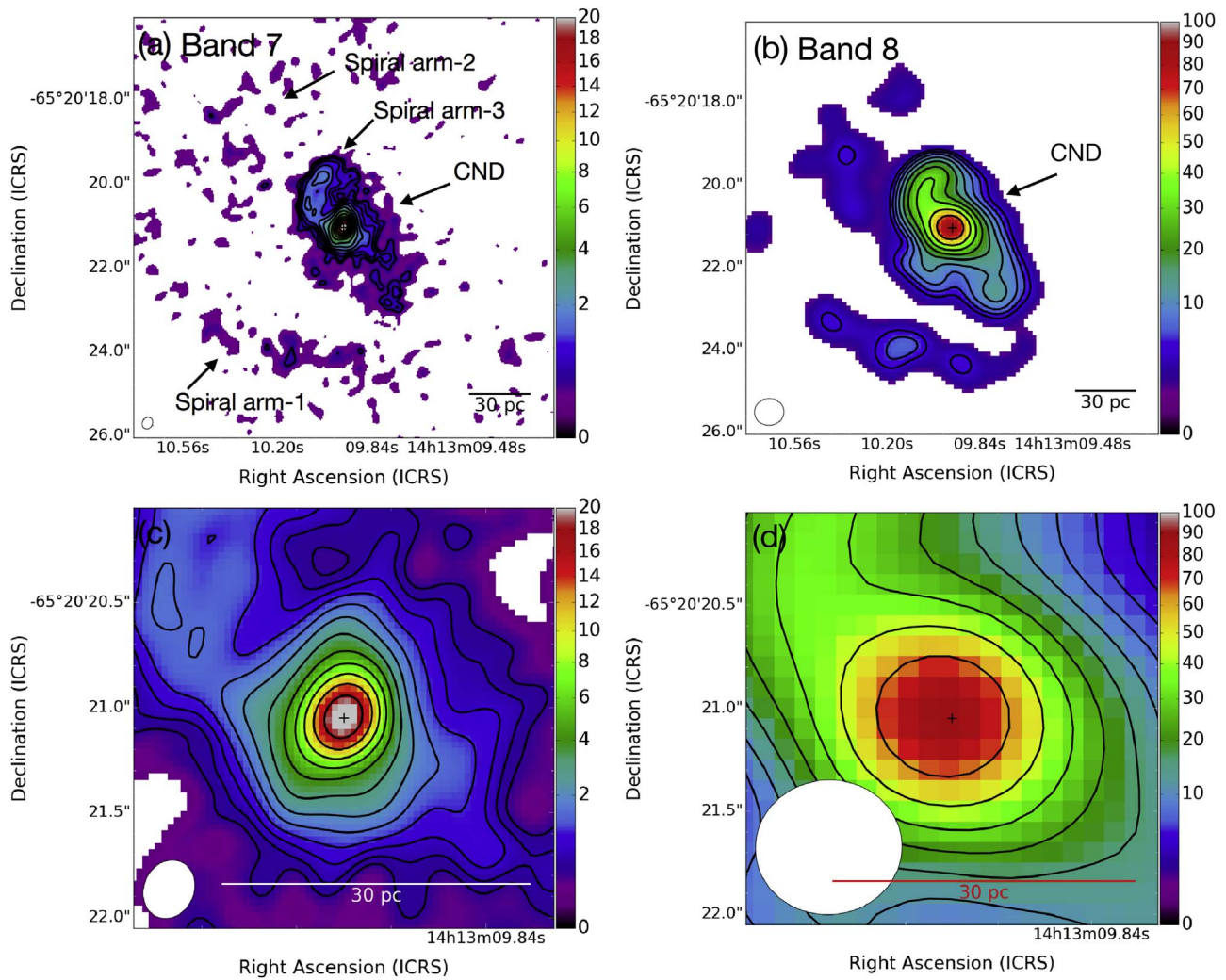


Figure 2. (a) Band 7 ($\nu_{\text{rest}} = 351$ GHz, $\lambda_{\text{rest}} = 854$ μm) continuum emission in the central $10'' \times 10''$ region of the Circinus galaxy, shown in both color scale (mJy beam^{-1}) and contours ($5 \times 2^{(n-1)/2} \sigma$ with $n = 1, 2, \dots$, and 12, where $1\sigma = 0.075$ mJy beam^{-1}). (b) Band 8 ($\nu_{\text{rest}} = 485$ GHz, $\lambda_{\text{rest}} = 618$ μm) continuum emission in the same region as shown in (a). The contours indicate $5 \times 2^{(n-1)/2} \sigma$ with $n = 1, 2, \dots$, and 9, where $1\sigma = 0.80$ mJy beam^{-1} . (c) Zoomed-in view of the central $2'' \times 2''$ of (a). (d) Zoomed-in view of the central $2'' \times 2''$ of (b). In each panel, the central plus sign marks the AGN position and the synthesized beams are shown as a white ellipse. These maps were constructed with Briggs weighting (robust = 0.5), without correcting the primary beam attenuations.

3.4. The Polar Elongation

To further investigate the detailed spatial distribution of the submillimeter continuum emission, we applied the UVMULTIFIT procedure (Martí-Vidal et al. 2014) to the Band 7 continuum visibility data, in which we have sampled long uv distance visibilities denser than the case of the Band 8 data. This model fitting method to the direct interferometric observable (visibility) is preferable to avoid systematic uncertainty in the image plane fitting due to, e.g., a nonlinear deconvolution algorithm, particularly when we fit beam-unresolved components.

The achieved visibility data is shown in Figure 4(a) as a function of uv distance (UVD), after averaging the visibilities over the observation time and frequency (representative frequency = 350.2 GHz). The almost constant amplitude at the $\text{UVD} \gtrsim 600$ k λ manifests the existence of a compact component, while the short UVD components reflect spatially extended structures. Here, we performed a two-dimensional double Gaussian fit to this visibility data: the use of double components is motivated by the existence of a parsec-scale

MIR polar elongation (Tristram et al. 2007, 2014), in addition to the extended CND seen in Figure 2. The results of the fit are summarized in Table 3 and the corresponding model is displayed in Figure 4(a) as well. As expected in the above, our best fit indeed supports the existence of a compact component at the AGN position (Component-1 in Table 3), in addition to the apparently extended structure (Component-2). The latter would correspond to a bright part of the CND (see also Figure 2). The fact that Component-2 is brighter than Component-1 is consistent with the prediction of our multiphase dynamic torus model that cold dust visible at longer FIR to submillimeter wavelengths is predominantly located in an extended disk, while more centrally concentrated components including warm dusty outflows are prominent at shorter NIR to MIR wavelengths (Schartmann et al. 2014). Note that, however, we also found that the residual amplitude remains high at the short UVD ($\lesssim 400$ k λ ; Figure 4(b)). This is due to the fact that there are some other spatially extended circumnuclear dusty structures in Circinus (e.g., spiral arms; Figure 2). As we would like to focus on the very nuclear structures in this subsection, fitting all components is beyond our scope.

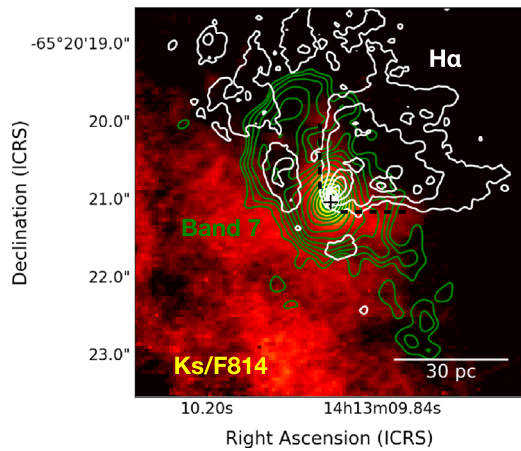


Figure 3. Overlay of the Band 7 continuum map (as shown in Figure 2; green contours) on the $K_s/F814$ flux ratio map (color scale; brighter regions denote those with higher ratios, Mezcua et al. 2016). The $K_s/F814$ ratio distribution around the AGN position delineates the boundary of the V-shaped $H\alpha$ emission line distribution (white contours; 0.1, 0.2, 0.4, 0.6, ..., and 1.0 in units of counts s^{-1} pixel $^{-1}$). The spiral-like structure seen in the Band 7 continuum emission traces the region that is radially farther than the very nuclear warm dust structure seen in the $K_s/F814$ ratio map (black dashed lines).

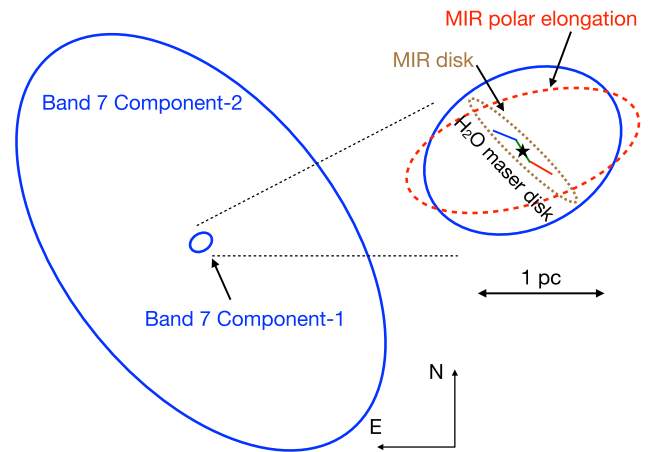


Figure 5. Schematic picture of the nuclear obscuring structures in the Circinus galaxy. Components 1 and 2 revealed by our ALMA Band 7 continuum observations are denoted by the blue ellipses. The central ~ 1 pc region is zoomed-in on the right side. Also plotted are the MIR disk (brown short-dashed line ellipse), the MIR polar elongation (red dashed line ellipse, Tristram et al. 2014), and the 22 GHz H_2O maser disk (central solid line, colors represent the line-of-sight velocity structure, Greenhill et al. 2003), respectively.

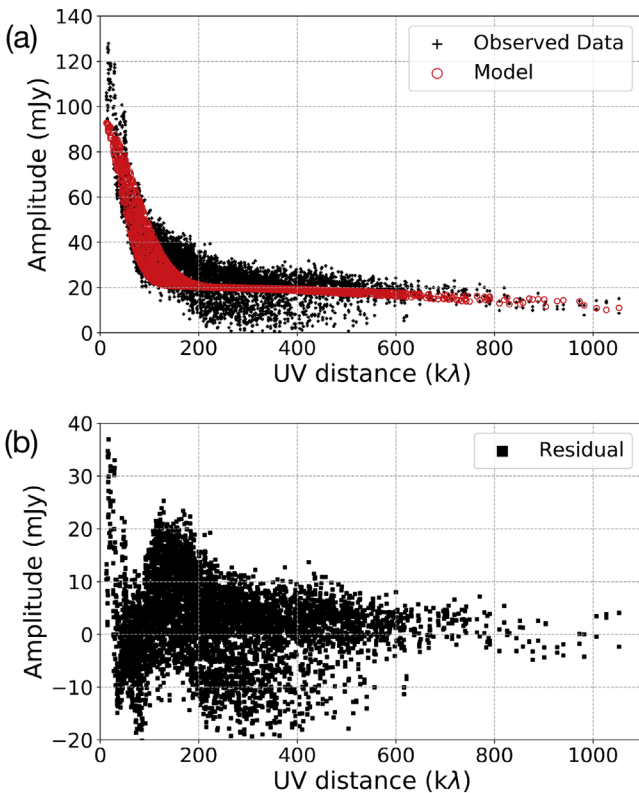


Figure 4. (a) ALMA uv distance vs. amplitude plot of the Band 7 continuum data of the Circinus galaxy (black). The model visibility data of our double Gaussian fit, returned by the UVMULTIFIT task, is also shown (red). (b) Residual visibility amplitude of the Band 7 continuum data, after subtracting the model component, shown as a function of uv distance.

The spatial distributions of several (circum)nuclear major components that we are interested in are illustrated in Figure 5. The axis ratio of Component-2 suggests that this structure is moderately inclined if it is a circular disk ($\simeq 55^\circ$). This inclination angle is slightly smaller than the galactic-scale one

Table 3

Results of the Visibility Modeling (Band 7)

	Component-1	Component-2
Major axis (mas)	80 ± 13	1634 ± 34
Minor axis (mas)	60 ± 6	951 ± 21
Major axis (pc)	1.6 ± 0.3	33.3 ± 0.7
Minor axis (pc)	1.2 ± 0.1	19.4 ± 0.4
PA ($^\circ$)	298 ± 21	218 ± 1.4
Integrated flux (mJy)	20.7 ± 1.3	73.5 ± 1.6

Note. The two-dimensional double Gaussian fit shown here was performed with the CASA task UVMULTIFIT. Both components have a centroid consistent with the AGN position.

($\simeq 65^\circ$) possibly because the spatially extended/elongated emission along the northeast–southwest direction, particularly at the southwestern side of the nucleus, is faint (see also Figure 2(a)). This will decrease the inclination angle with our simple method. Such an extended structure is clearly recognized in, e.g., the CO(3–2) integrated intensity map (Section 4), which indeed yields a better agreeing inclination angle with the above-mentioned galactic-scale one. Meanwhile, Component-1 appears elongated along the *polar direction* of the H_2O maser disk. This immediately brings to mind the parsec-scale MIR polar elongation (Tristram et al. 2014). The derived source size (1.6 ± 0.3 pc \times 1.2 ± 0.1 pc) and PA ($298^\circ \pm 21^\circ$) of Component-1 are roughly consistent with those of the MIR polar elongation (~ 1.9 pc and $\sim 287^\circ$, respectively). Therefore, we suggest that Component-1 traces the same physical structure as the MIR polar elongation. Although we need higher-resolution direct imaging to robustly reveal this compact structure, our finding here will support the actual existence of such elongated structures at the hearts of AGNs (e.g., López-Gonzaga et al. 2016), which created a new challenge to the classic torus paradigm.

4. Gas Distributions and Line Ratios

In this section, we analyze the unprecedented high-resolution CO(3–2) and [C I](1–0) emission line data of Circinus and then

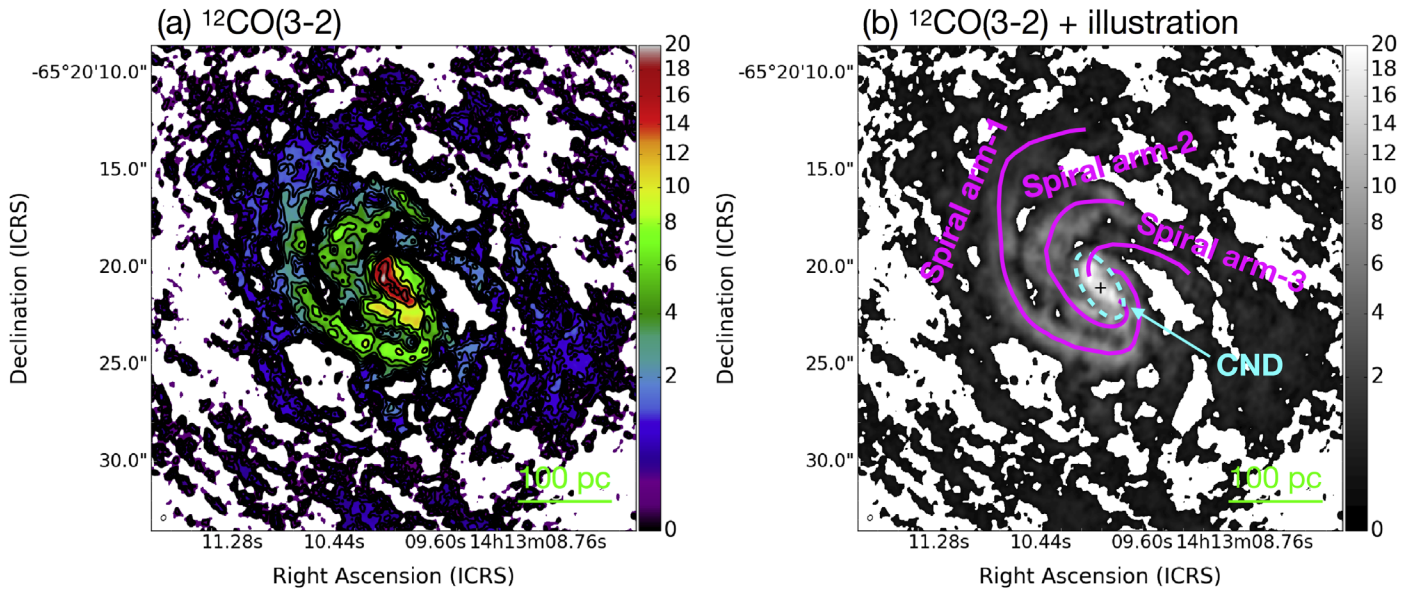


Figure 6. (a) The global integrated intensity map of CO(3–2) in the central $25'' \times 25''$ (or $\sim 500 \text{ pc} \times 500 \text{ pc}$) box of the Circinus galaxy, shown in both color scale ($\text{Jy beam}^{-1} \text{ km s}^{-1}$) and contours ($5 \times 2^{(n-1)/2} \sigma$ with $n = 1, 2, \dots, \text{and } 15$, where $1\sigma = 0.026 \text{ Jy beam}^{-1} \text{ km s}^{-1}$ or 3.8 K km s^{-1}). The synthesized beam ($0''.29 \times 0''.24$) is shown at the bottom left corner as a small white ellipse. The primary beam attenuation is uncorrected. The AGN position is indicated by a black plus sign. (b) The same as (a), but displayed in grayscale. The supposed galactic-scale major molecular structures (i.e., three spiral arms and the CND) are illustrated. Note that the southeastern side is the near side of this galaxy.

discuss their spatial distributions. Our analysis reveals that the bulk of these emission come from the innermost $10''$ region, although the missing flux is considerable. Here, the CASA task `IMMOMENTS` was used to generate the 0th moment maps without any clipping: the emission has been integrated over $V_{\text{LSR}} = 200\text{--}700 \text{ km s}^{-1}$, which is sufficient to cover their full velocity ranges (see also Figure 11).

4.1. CO(3–2) map

Figure 6(a) shows the CO(3–2) velocity-integrated intensity map of Circinus, over the central $25''$ ($=500 \text{ pc}$) region. The structures seen here are the counterparts to the postulated 300 pc-radius ring or disk in Elmouttie et al. (1998b). After convolving the map to an $18''$ aperture and correcting for the primary beam attenuation, we found that a roughly $\sim 50\%$ of the total CO(3–2) line flux has been resolved out compared to the APEX single-dish data (Zhang et al. 2014). As for the dust continuum emission, we identify two main structures in this circumnuclear region through closer inspection of the map: these are illustrated in Figure 6(b). A zoomed-in view (central $10'' = 200 \text{ pc}$) is shown in Figure 7(a). We describe each structure below.

4.1.1. Spiral Arms

Three possible spiral arms (labeled 1, 2, and 3 in Figure 6(b)) are visible. These could be inner extensions of the arms seen in the larger-scale CO(1–0) map (Zschaechner et al. 2016). In addition, inter-arm spur or feather structures also appear, as is the case in the nearby grand-design spiral galaxy M51 (e.g., Schinnerer et al. 2013). Meanwhile, the gaseous bar at the southeast of the nucleus (Maiolino et al. 2000) cannot be identified: the relatively straight-aligned CND and bright knots in spiral arms 1 and 2 at the southeastern region of the nucleus (Figure 7(a)) could have been mistaken as a bar.

Given the high critical density of CO(3–2), $n_{\text{crit}} = 5 \times 10^4 \text{ cm}^{-3}$ (for a temperature of 100 K, Kaufman et al. 1999),

one would expect that several bright *knots* in the spiral arms (Figure 7(a)) are the sites of star formation: each knot typically has a size of a few to $\sim 10 \text{ pc}$, and thus can be classified as a molecular cloud. Then, the spatial distributions of the CO(3–2) and the $\text{H}\alpha$ (Section 2) are compared in Figure 7(b). At spiral arms 2 and 3, where the $\text{H}\alpha$ emission is weakly visible, there were no good spatial coincidences between the CO-bright knots/regions and the $\text{H}\alpha$ -bright regions. Therefore, as is naively expected, this $\text{H}\alpha$ emission only traces unobscured star formation. Another finding is that spiral arm 1 clearly traces the $\text{H}\alpha$ dark lane at the southeastern side (near side) of this galaxy (Wilson et al. 2000). If we suppose that typical CO(3–2) emission along the spiral arm 1 ($\sim 4 \text{ Jy beam}^{-1} \text{ km s}^{-1}$) is thermalized with that of CO(1–0), we would expect there to be visual extinction of $A_V \sim 120 \text{ mag}$, by applying the standard Galactic CO conversion factor and the extinction law.¹⁴ This is one order of magnitude higher than that estimated from the $R\text{--}H$ and $H\text{--}K$ color map analyses (Maiolino et al. 2000), and thus is sufficient to create the dark lane.

4.1.2. The CND

The spiral arms converge to, or jointly constitute, a bright and compact gas concentration at the center, i.e., the CND, which appears as an inclined disk. A two-dimensional Gaussian fit to the central $3'' \times 3''$ area on the image plane (CASA task `IMFIT`) estimates the beam-deconvolved distribution as $(3''.62 \pm 0''.15) \times (1''.66 \pm 0''.07)$ or $(74 \pm 3) \text{ pc} \times (34 \pm 1) \text{ pc}$ with $\text{PA} = 212^\circ 0 \pm 1^\circ 9$. The derived PA here (and that of the Component-2 found in the Band 7 continuum emission distribution) is entirely consistent with those on the galactic $> \text{kpc}$ scale, e.g., HI emission and CO(1–0) emission distributions ($\sim 210^\circ$, e.g., Freeman et al. 1977; Curran et al. 1998), as well as that of the nuclear H_2O maser disk (209° at $r = 0.1 \text{ pc}$

¹⁴ $X_{\text{CO}(1-0)} = 2 \times 10^{20} \text{ cm}^{-2} (\text{K km s}^{-1})^{-1}$ from Bolatto et al. (2013) and $A_V/N_H = 5.3 \times 10^{-22} \text{ mag cm}^2$ from Draine (2011).

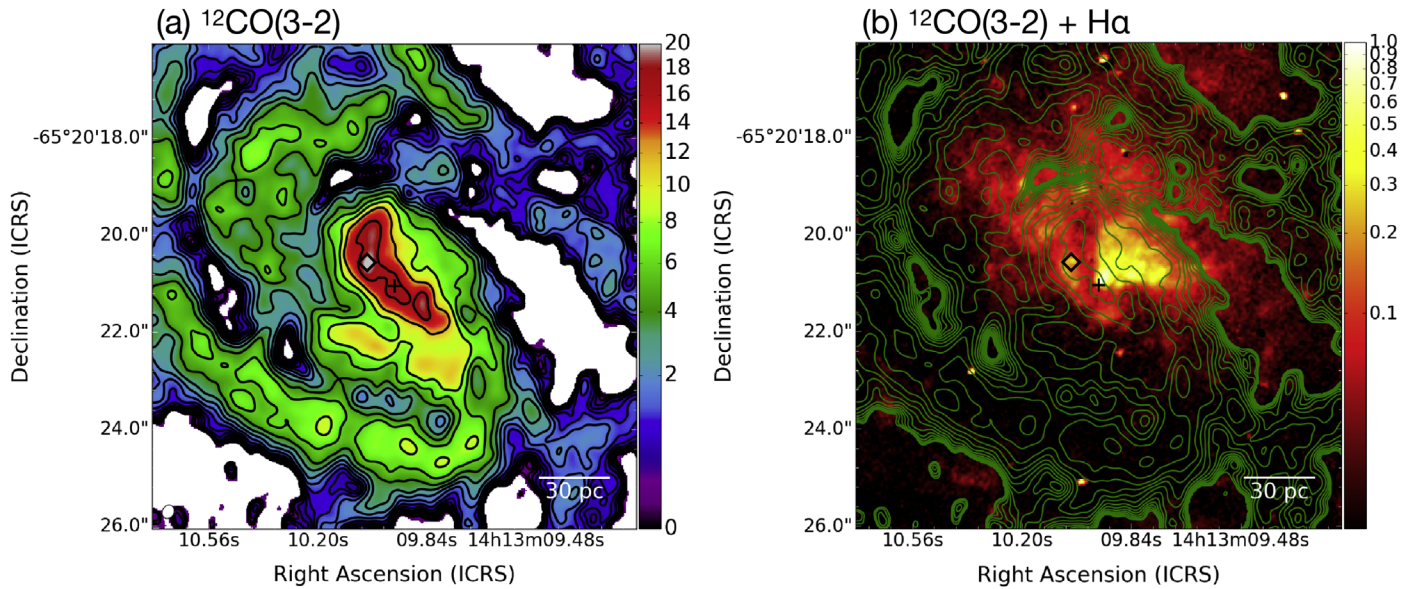


Figure 7. (a) A zoomed-in view of Figure 6(a) at the central $10'' \times 10''$ (or $\sim 200 \times 200$ pc²) box, shown in both color scale ($\text{Jy beam}^{-1} \text{ km s}^{-1}$) and contours ($5 \times 2^{(n-1)/2} \sigma$ with $n = 1, 2, \dots$, and 15, where $1\sigma = 0.026 \text{ Jy beam}^{-1} \text{ km s}^{-1}$ or 3.8 K km s^{-1}). The synthesized beam ($0''.29 \times 0''.24$) is shown at the bottom left corner as a white ellipse. The primary beam attenuation is uncorrected. (b) Overlay of the CO(3–2) distribution (contours; levels as in panel (a)) on the H α image (color scale in units of counts $\text{s}^{-1} \text{ pixel}^{-1}$). In each panel, the central plus sign indicates the AGN location, whereas the diamond indicates the peak position of the CO(3–2) integrated intensity.

and 236° at $r = 0.4$ pc; Greenhill et al. 2003). An inclination angle estimated from the above deconvolution, by assuming that the molecular gas is distributed in a circular disk, is $\simeq 63^\circ$. This angle is again fully consistent with that of the galactic-scale H I gas distribution, but is smaller than that of the nuclear MIR disk ($>75^\circ$, Tristram et al. 2014). The global inclination angle we obtained is also smaller than that ($\sim 75^\circ$) required in Wada et al. (2016) to reproduce the continuum SED of Circinus with the multiphase dynamic torus model. One plausible and simple explanation is that the CND of Circinus is warped from the center (i.e., the edge-on disk seen as the H₂O maser disk, Greenhill et al. 2003) to the outward edge. This is in agreement with the observation that the orientation of a large-scale gas/stellar distribution is unrelated to that of the radio jet, i.e., the polar direction of a presumed torus (Clarke et al. 1998; Nagar & Wilson 1999).

We found good spatial coincidence between the Band 7 continuum distribution and the CND. Thus, the CND also delineates the outer boundary of the warm dust structure (Mezcua et al. 2016), which would collimate the H α emission, as shown in Section 3. Note that we suppose that the northwestern part of spiral arm 2 (see also Figure 6(b)) is at the far side with respect to the H α cone: otherwise, the cone is obscured by cold dusty gas. The apex of the H α cone barely appears because this CND is inclined. Meanwhile, the other side (i.e., southeastern side) of the H α cone is completely obscured by the CND, although that side is partially visible at longer wavelength emission lines such as Pa α (Maiolino et al. 2000; Mezcua et al. 2016).

Owing to the much higher S/N (Table 2) than the Band 7 continuum map, our CO(3–2) integrated intensity map reveals a wealth of detail in this CND. The gas distribution there is not uniform with the off-centered peak position ($20.8 \text{ Jy beam}^{-1} \text{ km s}^{-1}$; marked as the diamond in Figure 7) at $\sim 1''$ northeast of the nucleus ($18.0 \text{ Jy beam}^{-1} \text{ km s}^{-1}$). This offset would be unaffected by spatial filtering given the much larger maximum recoverable scale ($\sim 7''$) of our observations

(Section 2). The spatial offset of the CO peaks with respect to the exact AGN position is consistent with the highly inhomogeneous nature of CO brightness distributions simulated with our multiphase dynamic torus model (Wada et al. 2018).

We estimate the molecular mass of the CND to be $M_{\text{H}_2} \simeq 3 \times 10^6 M_\odot$, as follows. Here, we define the extent of the CND as that of the above beam-deconvolved source size ($3''.62 \times 1''.66$, PA = 212.0°). We assume that the CO(3–2) emission there (integrated intensity = 805 Jy km s^{-1}) is thermalized with that of CO(1–0) and use the standard equation (Solomon & Vanden Bout 2005) to calculate its line luminosity as $L'_{\text{CO}(1-0)} = 3.85 \times 10^6 \text{ K km s}^{-1} \text{ pc}^2$. Then, by applying the canonical CO conversion factor in active environments ($\alpha_{\text{CO}(1-0)} = 0.8 M_\odot (\text{K km s}^{-1} \text{ pc}^2)^{-1}$, Downes & Solomon 1998; Bolatto et al. 2013), the above M_{H_2} is obtained. In the same manner, we also estimate the line-of-sight H₂ column density toward the AGN position from the CO(3–2) integrated intensity ($18.0 \text{ Jy beam}^{-1} \text{ km s}^{-1}$, or 2675 K km s^{-1}) as $N_{\text{H}_2} = 5.4 \times 10^{23} \text{ cm}^{-2}$. Note that we expect this N_{H_2} to remain the lower limit of the true line-of-sight column density due to beam dilution. For example, given the ~ 3 K brightness temperature of the Band 7 continuum emission at the AGN position, we may expect \gtrsim a few to even $\sim 10\times$ larger N_{H_2} if the true physical temperature of the cold dust is, e.g., $\gtrsim 30$ K (with a modest opacity). Moreover, if α_{CO} is larger than the above canonical value by a factor of ~ 4 – 5 , as expected in recent radiative transfer simulations of multiple CO lines (Wada et al. 2018), we will also obtain a correspondingly larger M_{H_2} and N_{H_2} . Thus, this CND would provide a significant fraction of the Compton-thick material toward the Circinus AGN $N_{\text{H}} = (6.6\text{--}10) \times 10^{24} \text{ cm}^{-2}$, Arévalo et al. 2014). This is consistent with the results of our multiphase dynamic torus model applied to Circinus (Wada et al. 2016), which required additional nuclear obscuration by the CND-scale cold ISM to the obscuration by the central warm ISM, to fully reproduce the SED of this AGN. Hence, we suggest that the CND indeed operates as a significant part of the nuclear obscurer.

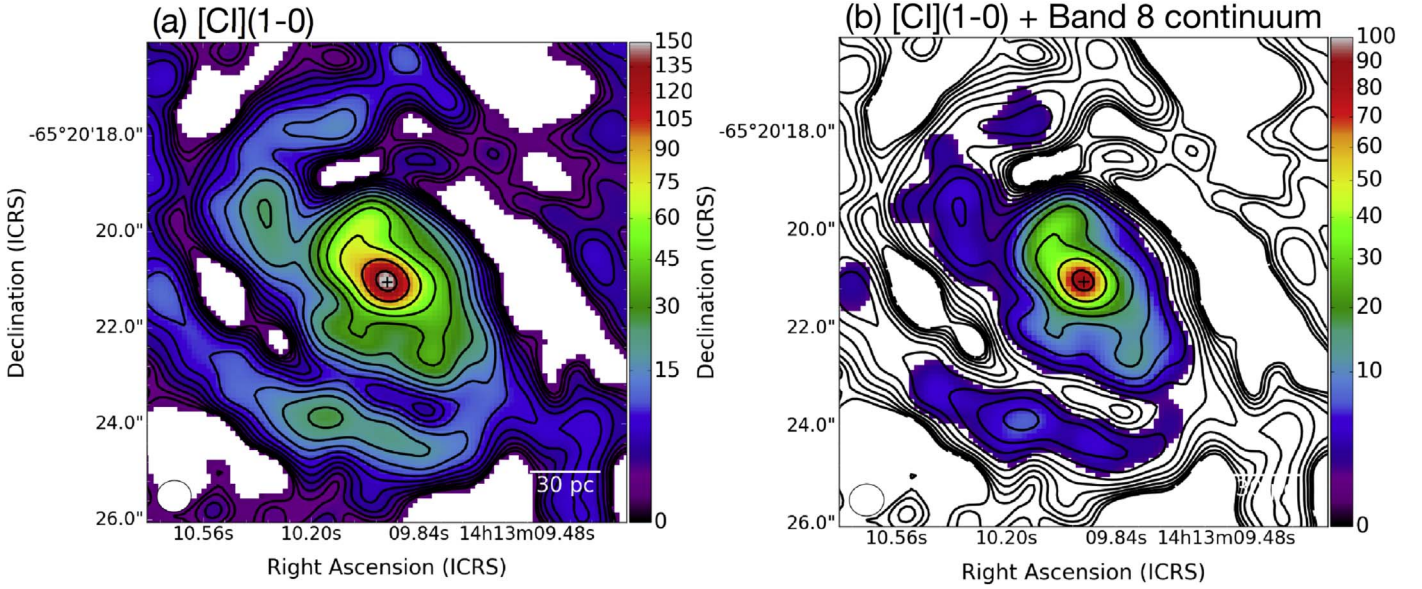


Figure 8. (a) Integrated intensity map of [C I](1–0) in the central $10'' \times 10''$ (or $\sim 200 \text{ pc} \times 200 \text{ pc}$) box of the Circinus galaxy, shown in both color scale ($\text{Jy beam}^{-1} \text{ km s}^{-1}$) and contours ($5 \times 2^{(n-1)/2} \sigma$ with $n = 1, 2, \dots, \text{and } 15$, where $1\sigma = 0.215 \text{ Jy beam}^{-1} \text{ km s}^{-1}$). The synthesized beam ($0''.71 \times 0''.66$) is shown at the bottom left corner as a white ellipse. The primary beam attenuation is uncorrected here. The AGN position is marked by a black plus sign. (b) The overlay of the [C I](1–0) integrated intensity (contours) on the Band 8 continuum map (color scale; same as in Figure 2(b)).

4.2. [C I] (1–0) map

The [C I](1–0) line emission is successfully detected both at the spiral arms and the CND (Figure 8(a)), with a clear peak at the AGN position ($154 \text{ Jy beam}^{-1} \text{ km s}^{-1}$). The [C I](1–0) distribution is consistent with that of the simultaneously obtained Band 8 continuum emission (Figure 8(b)). This [C I] (1–0) map shows the global distribution of cold and low-density (critical density $n_{\text{crit}} = 5 \times 10^2 \text{ cm}^{-3}$, Kaufman et al. 1999) gas in Circinus. It is difficult to estimate the missing flux for this [C I](1–0) observation, as the field of view of ALMA Band 8 ($12''.8$) is even smaller than the mapped area ($18''$) with APEX reported in Zhang et al. (2014). However, we found that our observation recovered 45% of that single-dish flux after correcting for the primary beam attenuation.

The overall resemblance of the [C I](1–0) distribution and the CO(3–2) distribution (Figure 9) supports the previous argument that [C I](1–0) essentially traces the same area as low- J CO lines, which has previously been reported for Galactic molecular clouds (e.g., Ikeda et al. 1999; Plume et al. 2000; Oka et al. 2005) and extragalactic objects (Krips et al. 2016; Miyamoto et al. 2018), and has been found in numerical models (e.g., Glover et al. 2015). However, we also found slight spatial inconsistencies in the detailed gas distributions, both at the spiral arms and the CND (Figure 9). Therefore, the [C I](1–0) also traces different gas volume from what the CO(3–2) does.

With regard to the spiral arms, we suggest that the spatial offsets ($\lesssim 10 \text{ pc}$) of the [C I](1–0) peaks and the CO(3–2) peaks are due primarily to excitation conditions, as CO(3–2) requires $\sim 100\times$ denser gas than [C I](1–0) to be excited. Miyamoto et al. (2018) also reported spatial offsets between [C I](1–0)-bright knots and CO(3–2)-bright knots in the circumnuclear starburst ring of NGC 613. Meanwhile, our particular interest in this paper is centered on the [C I](1–0) to CO(3–2) spatial offset inside the CND. The [C I](1–0) peaks exactly at the AGN location, while the CO(3–2) peak is $\sim 1''$

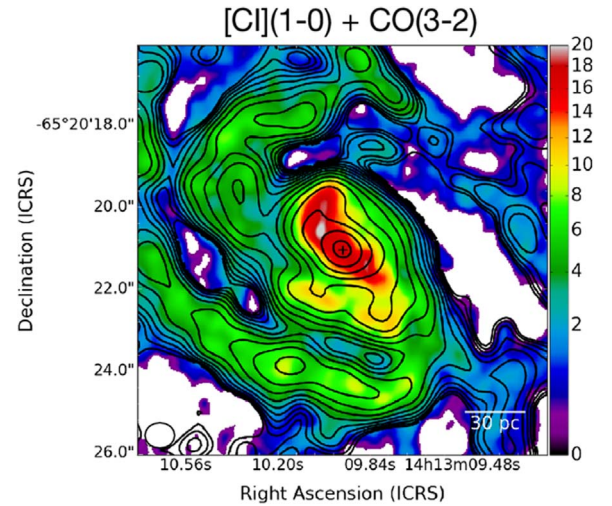


Figure 9. Superposition of the [C I](1–0) integrated intensity map (contours, as in Figure 8) on the CO(3–2) integrated intensity map (color scale, as in Figure 7), in the central $10'' \times 10''$ ($200 \text{ pc} \times 200 \text{ pc}$) of the Circinus galaxy. The central plus sign marks the AGN location. The synthesized beam of the [C I](1–0) cube is identified by the bottom left ellipse.

northeast of that position (Figure 9); this is discussed in more detail in Section 4.3.

We also performed a first-order estimate of M_{H_2} from the [C I](1–0) line luminosity ($L'_{\text{C I}(1-0)}$) at the CND, defined by the beam-deconvolved source size ($3''.62 \times 1''.66$) from the CO(3–2) analyses (Section 4.1). The obtained value there is $1.42 \times 10^6 \text{ K km s}^{-1} \text{ pc}^2$. We first estimate the atomic carbon mass ($M_{\text{C I}}$) by following Ikeda et al. (2002) and Weißel et al. (2005) as,

$$M_{\text{C I}} = 5.71 \times 10^{-4} Q(T_{\text{ex}}) \frac{1}{3} e^{23.6/T_{\text{ex}}} L'_{\text{C I}(1-0)} [M_{\odot}], \quad (1)$$

where $Q(T_{\text{ex}}) = 1 + 3e^{-T_1/T_{\text{ex}}} + 5e^{-T_2/T_{\text{ex}}}$ is the CI partition function, $T_1 = 23.6$ K and $T_2 = 62.5$ K are the level energies above the ground state, and T_{ex} is the excitation temperature. This equation assumes optically thin line emission under the LTE condition.

Even under the LTE condition, we would need to correct for line opacity, as there is no guarantee that the [C I](1–0) line emission in Circinus is optically thin. However, we expect that its line opacity is moderate ($\tau_{\text{CI}(1-0)} \lesssim 1$) given its peak line intensity (~ 1144 mJy beam $^{-1}$ or ~ 12.3 K) at the AGN position and its likely high T_{ex} such as $\gtrsim 30$ K (typical value observed in high-redshift quasars, Walter et al. 2011). If $\tau_{\text{CI}(1-0)} \lesssim 1$, then the correction factor for flux attenuation ($\tau_{\text{CI}(1-0)}/1 - \exp(-\tau_{\text{CI}(1-0)})$) is $\lesssim 1.6$, i.e., the Equation (1) gives a good estimate of M_{CI} . Then we achieve $M_{\text{CI}} \simeq 1770 M_{\odot}$ within the CND by assuming that $T_{\text{ex}} = 30$ K; this mass does not change significantly as long as $T_{\text{ex}} \gtrsim 30$ K. If we adopt a relative C I abundance with respect to H_2 as 8×10^{-5} , which is also the typical value observed in high-redshift quasars (Walter et al. 2011), we obtain M_{H_2} of $\simeq 3.7 \times 10^6 M_{\odot}$ in the CND. This is consistent with the CO(3–2)-based M_{H_2} derived in Section 4.1.2.

4.3. [C I](1–0)/CO(3–2) Line Ratio

Here, we discuss the [C I](1–0)/CO(3–2) integrated intensity ratio ($\equiv R_{\text{CI}/\text{CO}}$; brightness temperature scale) at both the CND and the spiral arms by comparing them with previous measurements in external galaxies and Galactic star-forming regions. We first adjust the uv range and the beam size of the CO(3–2) data to those of the [C I](1–0) data ($25\text{--}470$ k λ , $0''.71 \times 0''.66$ with PA = 96°). The resultant CO(3–2) cube has a 1σ sensitivity of 0.54 mJy beam $^{-1}$ at a velocity resolution of 10 km s $^{-1}$.

Figure 10 shows the $R_{\text{CI}/\text{CO}}$ in the central region of Circinus. The typical value of $R_{\text{CI}/\text{CO}}$ at the spiral arms is ~ 0.3 , although there are two spots with high ratios; we expect that the local gas densities there are too low to efficiently excite the CO(3–2) line. On the other hand, it is notable that the $R_{\text{CI}/\text{CO}}$ at the AGN position is ~ 3 times higher (~ 0.9) than the spiral arms. Given the much higher n_{crit} of CO(3–2) than that of [C I](1–0), this ratio would be hard to explain by simple gas excitation, as it would be naively expected that the gas density profile is centrally peaked. The same situation is also demonstrated in the line spectra (Figure 11): while the [C I](1–0) and the CO(3–2) show totally comparable line flux densities when measured at the central $10''$ box (i.e., CND + spiral arms), the [C I](1–0) emission clearly becomes brighter than the CO(3–2) emission at the AGN position. The relevant $R_{\text{CI}/\text{CO}}$ measured at several spatial scales are listed in Table 4; the high $R_{\text{CI}/\text{CO}}$ at the AGN position is uncommon in star-forming galaxies, which could be explained by an efficient CO dissociation due to hard X-ray irradiation from the AGN (XDR, Maloney et al. 1996; Meijerink & Spaans 2005).

Indeed, based on the one-zone XDR model of Maloney et al. (1996), we can estimate the X-ray energy deposition rate per particle (H_X/n) with

$$H_X \sim 7 \times 10^{-22} L_{44} r_2^{-2} N_{22}^{-1} \text{ erg s}^{-1}, \quad (2)$$

where L_{44} is the 1–100 keV X-ray luminosity in units of 10^{44} erg s $^{-1}$, r_2 is the distance from the AGN to the point of interest in units of 100 pc, and N_{22} is the X-ray attenuating

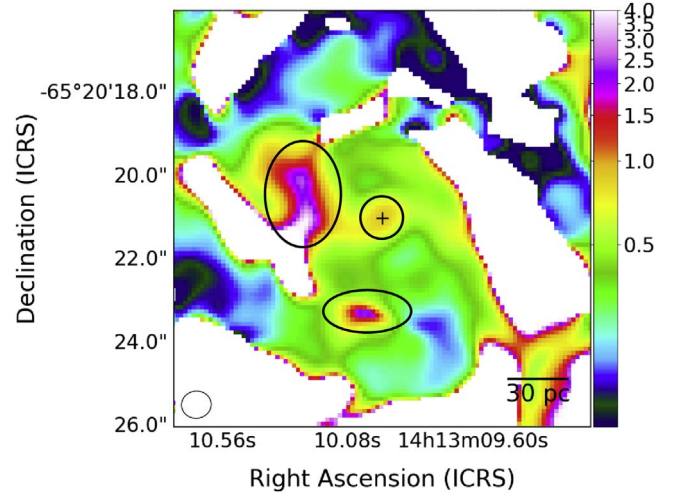


Figure 10. [C I](1–0) to CO(3–2) integrated intensity ratio map (brightness temperature scale) in the central $10'' \times 10''$ (200 pc \times 200 pc) of the Circinus galaxy. Three regions of high line ratio (black ellipses), one at the AGN position and two at the spiral arms, are highlighted for clarity. This map is made over the region where both the CO(3–2) and the [C I](1–0) integrated intensity maps show $S/N > 5$. Note that the uv - and beam size-matched CO(3–2) data are used here.

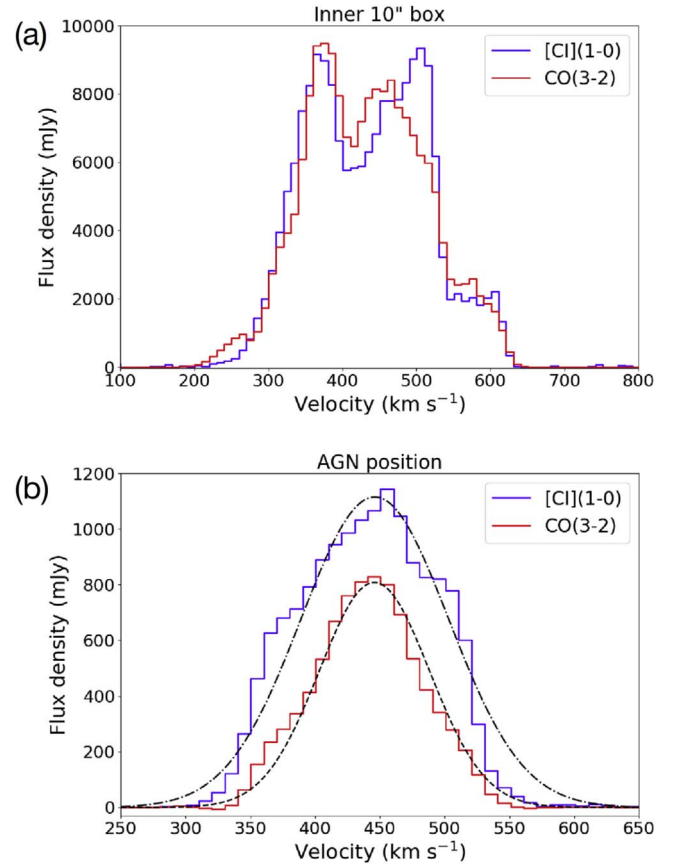


Figure 11. Line profiles of the [C I](1–0) and the CO(3–2) measured at (a) the inner $10'' \times 10''$ box and (b) the AGN location (with the single $0''.71 \times 0''.66$ beam) of the Circinus galaxy. The uv range and the beam size of the CO(3–2) data are matched to those of the [C I](1–0) data. The multiple-horn line profile in (a) is due to the spiral arms. The results of single Gaussian fits to the CO(3–2) and [C I](1–0) spectra at the AGN position (indicated by the dashed line and dotted-dashed line, respectively) are summarized in Table 5.

Table 4
The [C I](1–0)/CO(3–2) Line Ratio

	AGN	CND	10'' box
Jy km s ⁻¹	1.80 ± 0.25	1.03 ± 0.15	0.97 ± 0.14
K km s ⁻¹	0.89 ± 0.13	0.51 ± 0.07	0.48 ± 0.07

Note “AGN” indicates that the ratio is measured at the exact AGN location with the single [C I](1–0) synthesized beam (0.''71 × 0.''66). “CND” refers to the 3.''62 × 1.''66 (PA = 212°) region defined in the CO(3–2) map (Section 4.1.2). The 10'' box contains both the CND and the spiral arms. The 10% absolute flux uncertainties are included here.

column density in units of 10²² cm⁻², respectively. Here, we adopted $L_{44} = 0.13$ (with a photon index = 1.31 and cut-off energy = 160 keV) from Arévalo et al. (2014), as well as $n_{\text{H}_2} = 10^5$ cm⁻³ as a typical value in the molecular part of CNDs of Seyfert galaxies (e.g., Izumi et al. 2013; Viti et al. 2014). Then, we estimated H_X/n at $r = 7$ pc from the center (i.e., the half-major axis of the [C I](1–0) synthesized beam) as $\log(H_X/n) = -27.3$. According to the models in Maloney et al. (1996), this is almost exactly the rate at which the fractional abundance of C I (X_{CI}) becomes equal to that of CO (X_{CO}). At the regions where $\log(H_X/n) > -27.3$, we can expect $X_{\text{CI}}/X_{\text{CO}} > 1$. Thus, we suggest that the molecular dissociation due to X-ray irradiation is significant at the close vicinity of the Circinus AGN, which could cause the high $R_{\text{CI/CO}}$ there.

However, the actual three-dimensional (3D) geometrical structure of the XDR requires careful consideration: it does not necessarily form a simple one-zone structure. Indeed, single Gaussian fits to the observed CO(3–2) and [C I](1–0) spectra measured at the AGN position (Figure 11(b) and Table 5) revealed that the [C I](1–0) spectrum has a wider full width at half maximum (FWHM) than the CO(3–2) spectrum, as well as deviated components from the single Gaussian profile at about ± 70 km s⁻¹ to the systemic velocity (446 km s⁻¹). Both of these imply that the [C I](1–0) emission also traces a different gas volume than the CO(3–2) emission. This is consistent with the multiphase dynamic torus model (Section 5 and 6), where the complex interplay of gas chemistry and dynamics indeed occurs. Furthermore, there could be several other possibilities that can cause high $R_{\text{CI/CO}}$, including severe self-absorption in the CO(3–2) line and very peculiar gas excitation conditions. Observations of multiple transition lines and multiple species, including isotopologues, are required to better understand the origin of this enhancement.

Finally, we compare the $R_{\text{CI/CO}}$ of Circinus measured with three apertures with those of other galaxies (compiled from Zhang et al. 2014) in Figure 12. The comparison data consist of high-z quasar-host galaxies and submillimeter galaxies (Walter et al. 2011), as well as nearby galaxies, including NGC 6946 and M83 (Israel & Baas 2001), IC 342 (Israel & Baas 2003), Henize 2-10 and NGC 253 (Bayet et al. 2004), and M51 (Israel et al. 2006). As stated in Zhang et al. (2014), the $R_{\text{CI/CO}}$ of the nearby star-forming galaxies are ~ 0.1 to 0.2, while two AGN-host galaxies, M51 and Circinus (18'' aperture), show slightly higher values of ~ 0.3 , which already implies a sort of AGN influence on the line ratio. The averaged $R_{\text{CI/CO}}$ of the high-z objects is 0.32 ± 0.13 (Walter et al. 2011). As these are essentially starburst galaxies (e.g., Casey et al. 2014), one plausible explanation for the higher $R_{\text{CI/CO}}$ compared to nearby

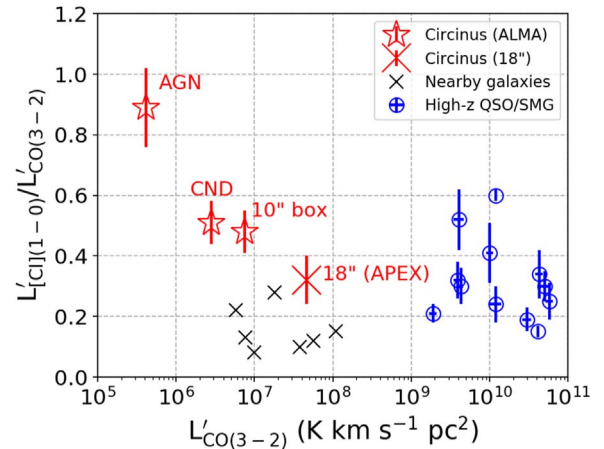


Figure 12. [C I](1–0)/CO(3–2) line ratio as a function of CO(3–2) line luminosity in units of the brightness temperature. The red star indicates the ratios in the Circinus galaxy, measured with three apertures in our ALMA data, while the large red cross is the ratio measured with APEX (18'' = 370 pc aperture, Zhang et al. 2014). Also shown are high-redshift submillimeter galaxies and quasar-host galaxies ($\gtrsim 30$ kpc apertures with blue circles, Walter et al. 2011), as well as single-dish measurements of nearby galaxies (Israel & Baas 2001, 2003; Bayet et al. 2004; Israel et al. 2006; aperture sizes are several hundreds to ~ 1 kpc).

Table 5
Results of the Single Gaussian Fit

	Peak (mJy beam ⁻¹)	Centroid (km s ⁻¹)	FWHM (km s ⁻¹)
CO(3–2)	807.9 ± 0.9	445.8 ± 0.1	100.3 ± 0.1
[C I](1–0)	1115.1 ± 4.6	446.1 ± 0.1	134.3 ± 0.2

Note. These fits were performed for the spectra at the AGN position, measured with the single [C I](1–0) synthesized beam (Figure 11(b)).

galaxies is that their mean interstellar radiation field over the entire galaxy scale is as high as those of the central ~ 1 kpc of the nearby AGNs, which would also lead to efficient CO dissociation. Compared to those nearby and high-z samples, the increasing trend of $R_{\text{CI/CO}}$ toward the center of Circinus, which would imply XDR chemistry, is remarkable.

5. Molecular and Atomic Gas Dynamics

In this section, we model the dynamics of the cold and dense molecular gas probed by the CO(3–2) line and that of the more diffuse atomic gas probed by the [C I](1–0) line. Our aim is to investigate their difference, particularly at the CND scale or inside, which will be key to understanding the geometrical structure of the circumnuclear obscuring material around the AGN.

5.1. Global Patterns

First, we show the global gas dynamics (intensity-weighted line-of-sight velocity and velocity dispersion) probed by both the CO(3–2) and the [C I](1–0) emission lines in Figure 13. These maps were made with the CASA task IMMOMENTS with 10σ clipping to avoid noisy pixels. The patterns traced by the two lines are reasonably consistent with each other, although we would need to beam-deconvolve them to achieve the actual

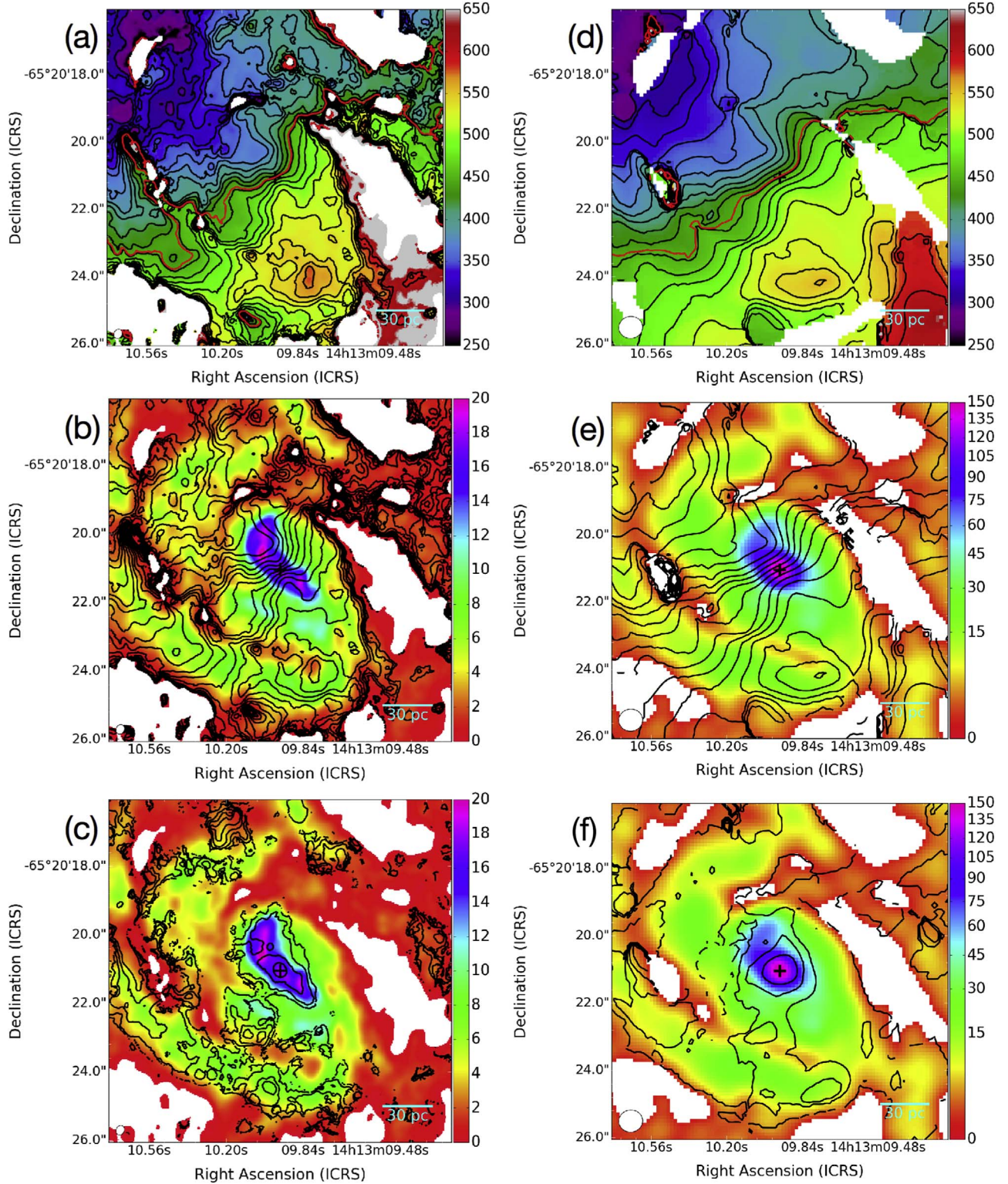


Figure 13. (a) Intensity-weighted mean velocity map of the CO(3–2) in the central $10'' \times 10''$ ($200 \text{ pc} \times 200 \text{ pc}$) box of the Circinus galaxy. The contours indicate the line-of-sight velocity of $300\text{--}600 \text{ km s}^{-1}$ in steps of 15 km s^{-1} . (b) The same contours as in (a), but superposed on the CO(3–2) integrated intensity map. (c) Intensity-weighted velocity dispersion (Gaussian sigma) map of the CO(3–2) shown by contours ($10\text{--}60 \text{ km s}^{-1}$ in steps of 10 km s^{-1}), superposed on the CO(3–2) integrated intensity map. (d)–(f) Similar to the left column, but for the cases of the [C I](1–0). The systemic velocity (446 km s^{-1}) estimated from our single Gaussian fit (Figure 11) is highlighted by the red line in both (a) and (d). The integrated intensities are shown in units of $\text{Jy beam}^{-1} \text{ km s}^{-1}$ and the central plus sign marks the AGN position.

gas dynamics (i.e., intrinsic rotation and dispersion; Section 5.2). The gas motion is clearly dominated by the galactic rotation with an overall northeast–southwest orientation (Figures 13(a), (d)),

which is consistent with previous studies at larger spatial scales (e.g., Curran et al. 2008; Zschaechner et al. 2016). On the other hand, it is also evident in the spiral arms that streaming motions

are superposed on the rotation pattern (Figures 13(b), (e)). These streaming motions, as well as spatial structures in each velocity channel (see the Appendix), may help the reader to recognize the likely three spiral arms that we have postulated and illustrated in Figure 6(b).

5.2. Decomposition with Tilted Rings

To extract basic beam-deconvolved dynamical information, particularly rotational velocity (V_{rot}) and dispersion (σ_{disp}), we fitted concentric tilted rings to the observed velocity structures with the ^{3D} Barolo code (Di Teodoro & Fraternali 2015). The main parameters were dynamical center, systemic velocity (V_{sys}), V_{rot} , σ_{disp} , galactic inclination (i), and PA, all of which can be varied in each ring. Here, we fixed the dynamical center to the AGN position and the V_{sys} to 446 km s^{-1} based on the single Gaussian fits to the observed nuclear spectra (Table 5); V_{rot} , σ_{disp} , i , and PA were thus the major free parameters and were evaluated by minimizing $|\text{model} - \text{observed data}|$. Given the significantly different spatial resolution between the CO(3–2) cube and the [C I](1–0) cube, we first present the results using the full-resolution CO(3–2) cube in Section 5.2.1 to describe the details of the gas dynamics as much as possible, and then present those with the uv - and beam-matched CO(3–2) and [C I](1–0) cubes in Section 5.2.2.

5.2.1. The CO(3–2) Full-resolution Data

The full-resolution CO(3–2) cube ($\theta = 0''.29 \times 0''.24$, $dV = 10 \text{ km s}^{-1}$) was used. We modeled 50 concentric rings with a separation of $\Delta r = 0''.15$, which is roughly half the size of the major axis of the synthesized beam. The modeled mean velocity field (moment 1) and the residual image after subtracting this model from the observed data are displayed in Figures 14(a) and (b), respectively. The residuals at the spiral arms are $\sim \pm 40 \text{ km s}^{-1}$ at arms 1 and 2, which are attributed to streaming motions. As the southeastern part is the near side of this galaxy (Wilson et al. 2000), these motions are likely inflows toward the vicinity of this AGN. Meanwhile, the residual is only a few km s^{-1} at the AGN position, which is consistent with our torus model tuned for Circinus (Wada et al. 2016), where the inflow velocity through the dense mid-plane of the CND is as slow as $\lesssim 10 \text{ km s}^{-1}$ (see also Figure 2 of Wada 2012).

Figures 15(a) and (b) present the modeled position–velocity diagrams (PVDs) along the global kinematic major and minor axes, respectively, overlaid on the observed PVDs. The overall structures are well reproduced by a combination of gas rotation and dispersion, although streaming motions are evident as well along the minor axis (offset $\sim 2''$ and $\sim 4''$), which positionally correspond to the spiral arms.

Figures 16(a), (b), and (c) show the radial profiles of the decomposed V_{rot} and σ_{disp} , i , and PA of our model, respectively. We found that variation in the i and the PA is small (within $\sim 15^\circ$) around $i \sim 65^\circ$ and PA $\sim 216^\circ$. These values are consistent with those on the galactic scale (e.g., Freeman et al. 1977; Elmouttie et al. 1998b). Nevertheless, we found a slight increasing trend in the i toward the AGN position. The inferred $i \gtrsim 70^\circ$ at $r \lesssim 10 \text{ pc}$ would be consistent with the $i > 75^\circ$ estimated for the 1 pc scale nuclear MIR disk (Tristram et al. 2014), as well as with the $i \sim 75^\circ$ required to reproduce the nuclear IR SED of this AGN based on our torus model (Wada et al. 2016). This increasing i will eventually

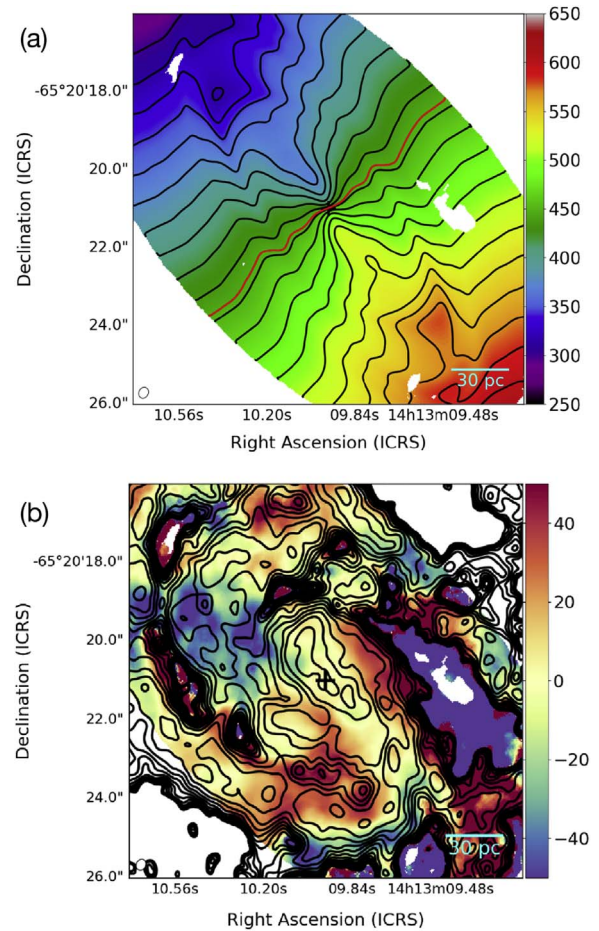


Figure 14. (a) Model velocity field (moment 1) of the Circinus galaxy. The contours are the same as in Figure 13(a). (b) Residual velocity image after subtracting the model from the observed data (color scale). The overlaid contours indicate the velocity-integrated CO(3–2) intensity as shown in Figure 7(a). The central plus sign marks the AGN location.

reach $\sim 90^\circ$ as Circinus hosts the 22 GHz H_2O maser disk at the center (Greenhill et al. 2003).

The radial profile of the $\sigma_{\text{disp}}/V_{\text{rot}}$ ratio is shown in Figure 16(d). This ratio can be considered as a scale height (H) to scale radius (R) ratio (H/R , i.e., the aspect ratio of a disk), under the hydrostatic equilibrium condition. From this panel, one can see that the $\sigma_{\text{disp}}/V_{\text{rot}}$ at $r \gtrsim 15 \text{ pc}$ is ~ 0.25 , while the ratio at the central $r \lesssim 10 \text{ pc}$ increases to ~ 0.4 (except for the innermost $r = 3 \text{ pc}$ ring, i.e., the dense molecular disk becomes geometrically thicker. Within the qualitative framework of our model, this moderate thickness of the dense gas disk at the central $\lesssim 10 \text{ pc}$ can be interpreted such that the dense gas and dust are puffed up due to the turbulence induced by the AGN-driven failed winds (Wada 2012; Wada et al. 2016, see Figure 1).

It is particularly noteworthy that the innermost $r = 3 \text{ pc}$ ring shows a very low $\sigma_{\text{disp}}/V_{\text{rot}} \sim 0.1$, which is not observed at the other radii. The implied very thin disk geometry, as well as the high i , would suggest that the geometrically thin Keplerian disk has finally started to be captured (i.e., the gas motion is governed by the gravity of the central SMBH) with this cold molecular emission line. Indeed, in the zoomed-in view of the radial profile of V_{rot} (Figure 16(e)), we found a turnover trend of V_{rot} at $r = 3 \text{ pc}$. Although the V_{rot} at that radius remains comparable to those at larger radii within uncertainties, it is

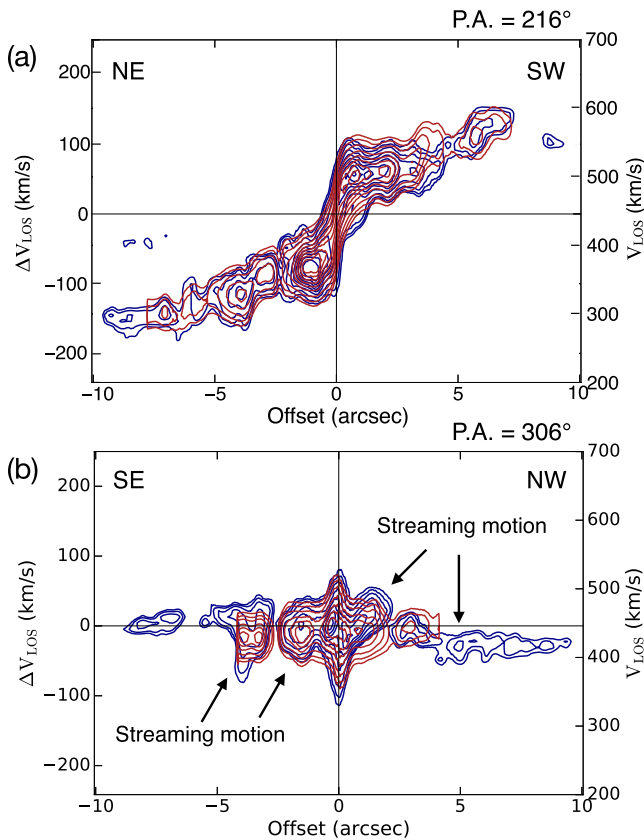


Figure 15. (a) The observed position–velocity diagram (PVD) of the CO(3–2) line along the major axis (PA = 216°) shown as the blue contours. The overlaid red contours indicate the PVD produced by our tilted ring model. Both contours are plotted at 25, 50, 75, 100, 200, ..., and 700 σ , where $1\sigma = 0.37$ mJy beam $^{-1}$. The full-resolution data ($\theta = 0''.29 \times 0''.24$) are used. (b) The PVD along the minor axis (PA = 306°). The same contours as in panel-(a) are shown. Due to the inclined geometry of the concentric rings, no model component exists at an offset $\gtrsim 5''$ (see also Figure 14(a)).

close to the extension of the nuclear Keplerian rotation curve around the central SMBH ($M_{\text{BH}} = 1.7 \times 10^6 M_{\odot}$), traced by the VLBI 22 GHz H₂O maser observations (Greenhill et al. 2003). Although it is difficult at this moment to achieve a firmer conclusion given the large errors associated with the inner rings, we can observe a clear difference in V_{rot} between e.g., $r = 1$ pc and $r = 3$ pc if the CO gas dynamics genuinely follow the Keplerian pattern. This can be tested with higher-resolution ALMA observations.

5.2.2. The uv - and Beam-matched Data

Next, we model the gas dynamics using the [C I](1–0) cube and the uv - and beam-matched CO(3–2) cube ($1\sigma = 0.54$ mJy beam $^{-1}$ at $dV = 10$ km s $^{-1}$). With this treatment, we expect to reduce the potential systematic effects on the resultant dynamical properties stemming from the unmatched uv ranges and beam sizes of the input data. Given the larger angular resolution ($0''.71 \times 0''.66$), we modeled only 20 concentric rings with $\Delta r = 0''.25$ and repeated the procedure in Section 5.2.1.

Figure 17(a) displays the resultant radial profiles of V_{rot} and σ_{disp} traced by the CO(3–2) and the [C I](1–0) emission lines. We found that both the V_{rot} and the σ_{disp} of the CO(3–2) derived here are consistent with those from the full-resolution CO(3–2) cube in Section 5.2.1. Thus, the $\sigma_{\text{disp}}/V_{\text{rot}}$ profile of

the CO(3–2) shown in Figure 17(b) is essentially the same as that in Figure 16(d). Furthermore, the V_{rot} and the σ_{disp} of the [C I](1–0) are consistent with those of the CO(3–2) derived here within uncertainties at most radii, except for the σ_{disp} at the innermost one ($0''.25 = 5$ pc). Considering our model, the similarity in the $\sigma_{\text{disp}}/V_{\text{rot}}$ ratios at $r \sim 10 - 20$ pc between the two tracers (Figure 17(b)) in turn suggests that the turbulence induced by the failed winds, which can act both on the atomic and molecular gas, plays a major role in determining the disk geometry there, i.e., the contribution from the outflows preferentially seen at ionized/atomic gas (Wada et al. 2016) would not be very significant. The commonly geometrically thin nature at $r \gtrsim 20$ pc, where the radiation-driven fountain will not work well for the case of Circinus (Wada et al. 2016), is also reasonable because SN feedback (an efficient mechanism to puff up the disk) should be weak given the low SFR ($\sim 0.1 M_{\odot} \text{ yr}^{-1}$; Esquej et al. 2014).

Meanwhile, the discrepancy of the $\sigma_{\text{disp}}/V_{\text{rot}}$ ratios at $r \lesssim 10$ pc (~ 0.15 in the CO(3–2) and ~ 0.4 in the [C I](1–0)) is more evident, which indicates the existence of multiphase dynamical structures around the AGN. Note that it is difficult to distinguish coherent outflow motion that can widen the line profile from isotropic turbulent motion due to failed winds, based simply on the observed σ_{disp} that mixes these motions. However, as the outflows are preferentially observed at ionized and/or atomic gas at the very nuclear region in our model (Wada et al. 2016), we expect that such outflows are the prime source of the geometrically thicker nature of the C I disk than the CO disk at this very central region. Indeed, we found that adding two more components (i.e., triple Gaussians) can fit the observed nuclear [C I](1–0) spectrum more faithfully, as shown in Figure 18 (see also Table 6). The central Gaussian component has almost the same centroid velocity and FWHM as the CO(3–2) spectrum (Table 5), suggesting that this traces the same region as the CO(3–2) line (the rotating disk mid-plane in our model). We also found that the blueshifted and redshifted components appear almost *symmetrically* with respect to the central component, with a velocity offset of ~ 75 km s $^{-1}$ (blue) and ~ 60 km s $^{-1}$ (red), respectively; this is suggestive of coherent atomic gas motion around the AGN. Therefore, these results support the view that the diffuse atomic gas is distributed in a geometrically thicker volume than the dense molecular gas around the AGN due to atomic outflows, as expected in our multiphase dynamic torus model. As this argument is rather qualitative, however, we perform a more quantitative comparison between the observed [C I](1–0) and CO(3–2) line properties and our model predictions in the next section.

6. Comparison with the Model

6.1. Line Intensities in Our Modeled Torus

To interpret the physical/dynamical nature of the circumnuclear obscuring structures from the observed line cubes, we used a snapshot of our multiphase dynamic torus model tuned for Circinus (Wada et al. 2016), where non-equilibrium XDR chemistry (Meijerink & Spaans 2005) was solved, to predict the emission line properties of multiple species.

The simulated CND has a circular gas distribution for simplicity with $r \simeq 16$ pc, with the total M_{H_2} of $2 \times 10^6 M_{\odot}$ (128^3 grids; 0.25 pc resolution), which is roughly consistent with the observed M_{H_2} in Circinus measured with a slightly

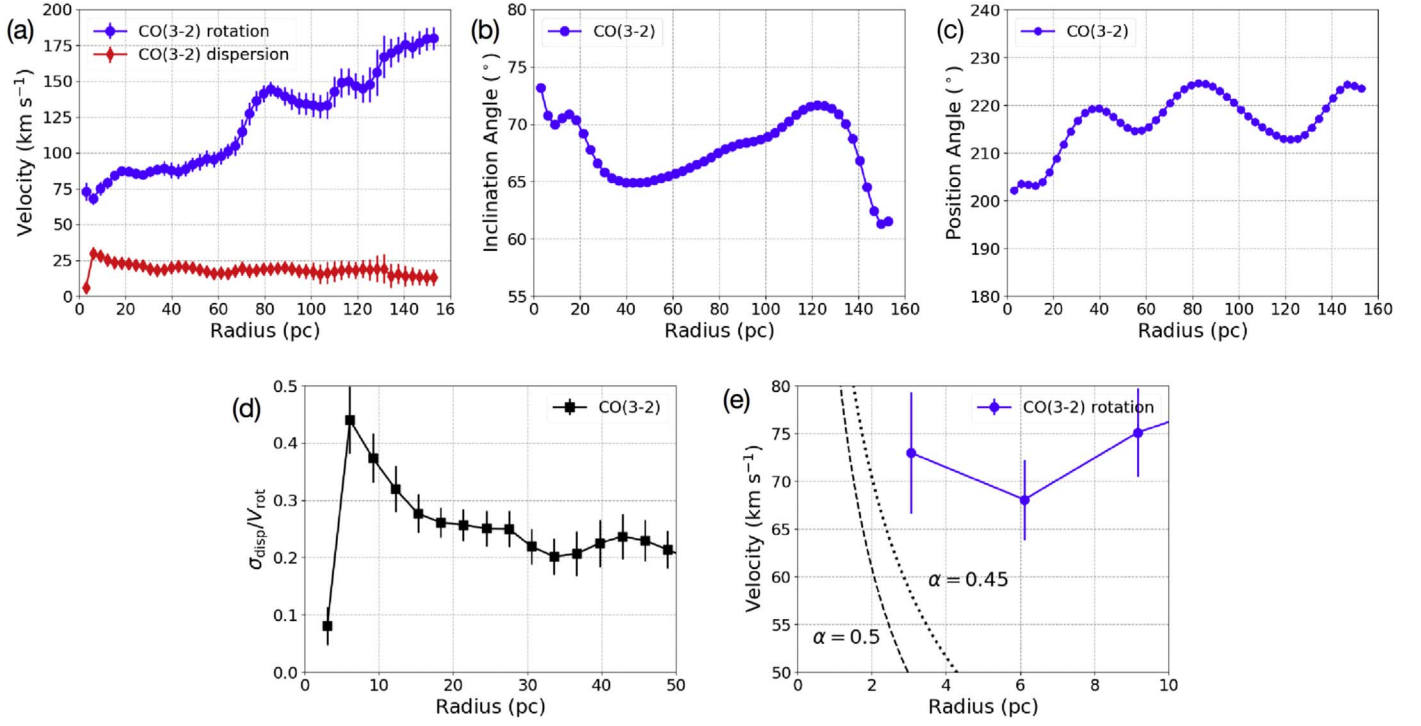


Figure 16. Radial profiles of (a) rotational velocity (V_{rot} ; blue circles) and velocity dispersion (σ_{disp} ; red diamonds), (b) inclination angle, and (c) position angle, estimated from our tilted ring model of the CO(3–2) velocity field of the Circinus galaxy. (d) The radial profile of the $\sigma_{\text{disp}}/V_{\text{rot}}$ ratio. (e) A zoomed-in view of the V_{rot} at the innermost 10 pc region. A turnover trend of the V_{rot} is suggested at $r \lesssim 5$ pc. Also plotted are the (quasi-) Keplerian motion ($V_{\text{rot}} \propto r^{-\alpha}$) with $\alpha = 0.5$ (dashed) and $\alpha = 0.45$ (dotted), inferred from the 22 GHz H₂O maser observations (Greenhill et al. 2003). The disk orbital velocity of 260 km s^{−1} at the innermost 0.11 pc of that maser disk is used for scaling.

larger aperture ($\sim 3\text{--}4 \times 10^6 M_{\odot}$ in the $r \sim 35$ pc disk with $\alpha_{\text{CO}} = 0.8 M_{\odot} (\text{K km s}^{-1} \text{pc}^2)^{-1}$; Section 4). The central AGN has the same M_{BH} and Eddington ratio as those observed (Section 1). The ultraviolet radiation from the central thin accretion disk is angle-dependent, whereas we assumed spherically symmetric X-ray radiation from the AGN corona. Self-gravity of the gas is ignored, as it is not essential for the dynamics in the fountain scheme (see also Wada 2012). After the XDR chemistry (abundance) was solved, post-processed non-LTE radiative transfer calculations were performed. Once the radiation field and optical depth are determined in each grid, we can observe line emission from an arbitrary direction (for further details see Wada et al. 2018). For example, Wada et al. (2018) presented the resultant properties of multiple ¹²CO transition lines from $J = 0$ to 15. Their procedure was fully applied to the case of the [C I](1–0) in this work.

6.2. Results of our Simulation

Figure 19 shows the edge-on distributions of the simulated integrated intensities of CO(3–2) and [C I](1–0) emission lines. This reinforces our argument that the diffuse atomic gas traced by the [C I](1–0) is more extended along the z -direction of the disk than the dense molecular gas traced by the CO(3–2) at this spatial scale ($r \lesssim 10$ pc), which is due to the atomic outflows in our model. On the other hand, one can recognize that the most intense part of the [C I](1–0) distribution essentially traces the same region as the CO(3–2) distribution. Note that the hydrogen (H₂ + H I) volume density in the disk mid-plane ($\sim 10^5 \text{ cm}^{-3}$) is $\gtrsim 100$ times higher than that of the spatially/vertically extended region ($\lesssim 10^3 \text{ cm}^{-3}$, Wada et al. 2016). Thus, the line-emitting region can be divided into the following two parts:

1. $|\Delta z| \lesssim 3$ pc: atomic gas and molecular gas coexist. Turbulence due to the failed winds determines the geometrical thickness of this region. The observed CO(3–2) line profile, as well as the central Gaussian component of the [C I](1–0) line profile (Figure 18), reflect this component.
2. $|\Delta z| \gtrsim 3$ pc: preferentially seen in the [C I](1–0) emission, not in the CO(3–2) emission. The AGN-driven outflows, which are selectively seen in the ionized and atomic gas phase, are responsible for producing this geometrically thick structure in the [C I](1–0) distribution.

Figure 20 shows simulated channel maps of (a) CO(3–2) intensity and (b) [C I](1–0) intensity at the systemic velocity of this galaxy with $i = 75^\circ$ (the best-fit value to reproduce the IR SED of Circinus with our model; Wada et al. 2016). For both the CO(3–2) and the [C I](1–0), the bulk of the emission comes from the region outlined by the CO(3–2) distribution. This region corresponds to the geometrically thin mid-plane of the CND, if viewed from the edge-on angle (Figure 19); therefore, we call this the inclined thin disk. Owing to the high inclination adopted here, we are still able to see the spatially extended (or vertically elongated along the z -direction due to outflows) component beside the inclined thin disk in the [C I](1–0) map (Figure 20(b)). As the outflows would have coherent velocities, we expect that blueshifted and redshifted components with such velocities can be superposed on a simple Gaussian profile in the simulated [C I](1–0) line profile, which is confirmed in the analysis below.

Figure 21(a) therefore exhibits how the [C I](1–0) and CO(3–2) line profiles appear when viewed with $i = 75^\circ$ based

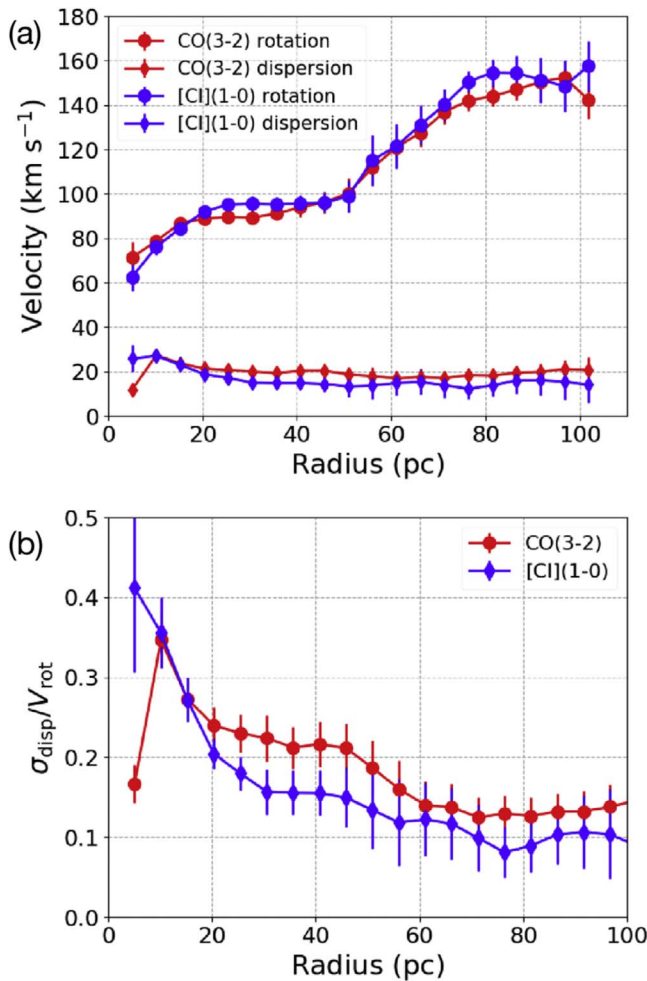


Figure 17. (a) Radial profiles of the rotational velocity (V_{rot} ; circles) and the velocity dispersion (σ_{disp} ; diamonds) derived from the CO(3-2) (red) and the [C I](1-0) (blue) emission lines, in the central $r \lesssim 100$ pc region of the Circinus galaxy. (b) Radial profiles of the $\sigma_{\text{disp}}/V_{\text{rot}}$ ratios traced by the CO(3-2) and the [C I](1-0) lines, at the same region as in (a). The uv ranges and the beam sizes are matched between the CO(3-2) cube and the [C I](1-0) cube here.

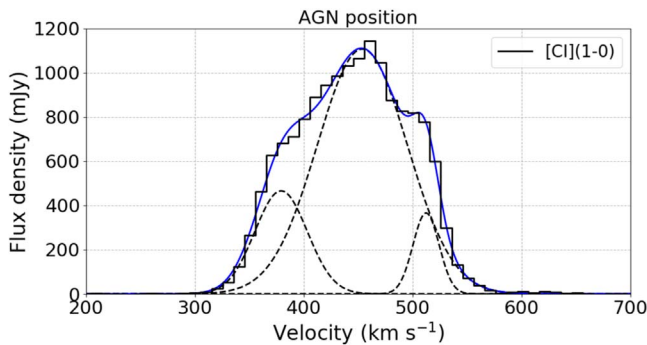


Figure 18. Line profile of the [C I](1-0) emission measured at the AGN position (with the single $0''.71 \times 0''.66$ beam) of the Circinus galaxy. A three-component Gaussian fit was performed; each component is indicated by the black dashed lines, and the total model is shown by the blue solid line. The derived line properties are listed in Table 6.

on our model (see also Table 7 for the results of the Gaussian fits). The simulated CO(3-2) profile that basically reflects the rotating mid-plane component of the inclined thin disk can be explained by a single Gaussian, as expected, whereas deviation

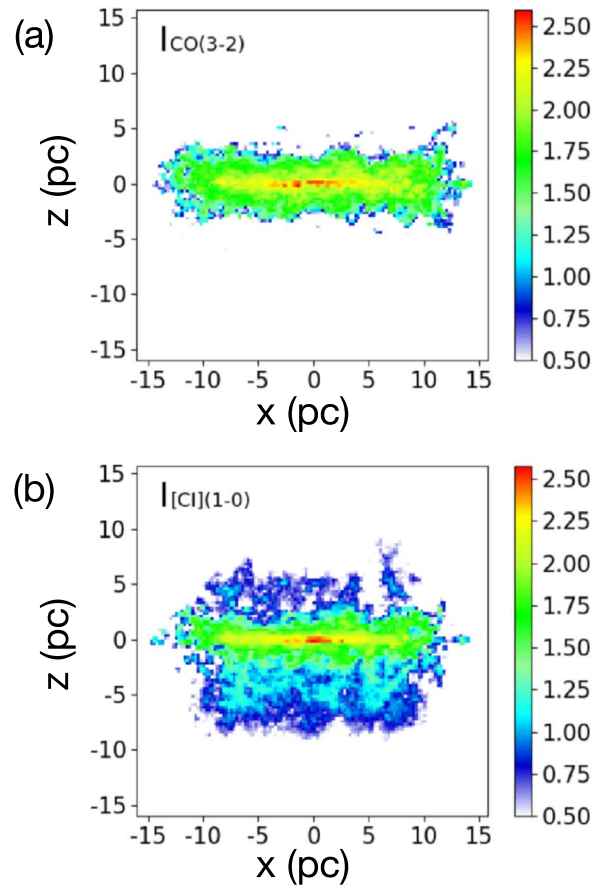


Figure 19. Simulated velocity-integrated brightness temperature maps of (a) CO(3-2) and (b) [C I](1-0) in the central region of the Circinus galaxy for $i = 90^\circ$ (edge-on), shown on a logarithmic scale. A simple circular disk geometry is assumed. The [C I](1-0) emission is spatially more extended along the z -direction than the CO(3-2).

Table 6
Results of the Three-component Gaussian Fit to the Observed [C I](1-0) Spectrum

	Peak (mJy beam ⁻¹)	Centroid (km s ⁻¹)	FWHM (km s ⁻¹)
Central	1107.9 ± 1.6	453.7 ± 5.6	97.7 ± 0.6
Blueshifted	466.4 ± 5.6	379.1 ± 0.2	56.7 ± 0.5
Redshifted	365.9 ± 4.4	512.3 ± 0.1	28.3 ± 0.4

Note. These fits were performed for the spectra at the AGN position, measured with the single synthesized beam ($0''.71 \times 0''.66$). The results of the single Gaussian fit are summarized in Table 5.

from a single Gaussian is evident in the case of the [C I](1-0) profile. The [C I](1-0) outflows are then clearly manifested in the three components Gaussian fit to the spectrum (Figure 21(b)). The blueshifted and redshifted features emerge at around the coherent outflow velocity of ~ 50 – 60 km s⁻¹ in our model. Hence, we here suggest that (i) this qualitative difference between the CO(3-2) and the [C I](1-0) line profiles, i.e., the existence of the additional two components to the single Gaussian profile in the case of the [C I](1-0), as well as (ii) the centroid velocities of these outflow components, are consistent with the observed profiles (Figure 11(b) and 18). Note that the amplitudes of the model components are smaller than, and the relative strengths among the three [C I](1-0)

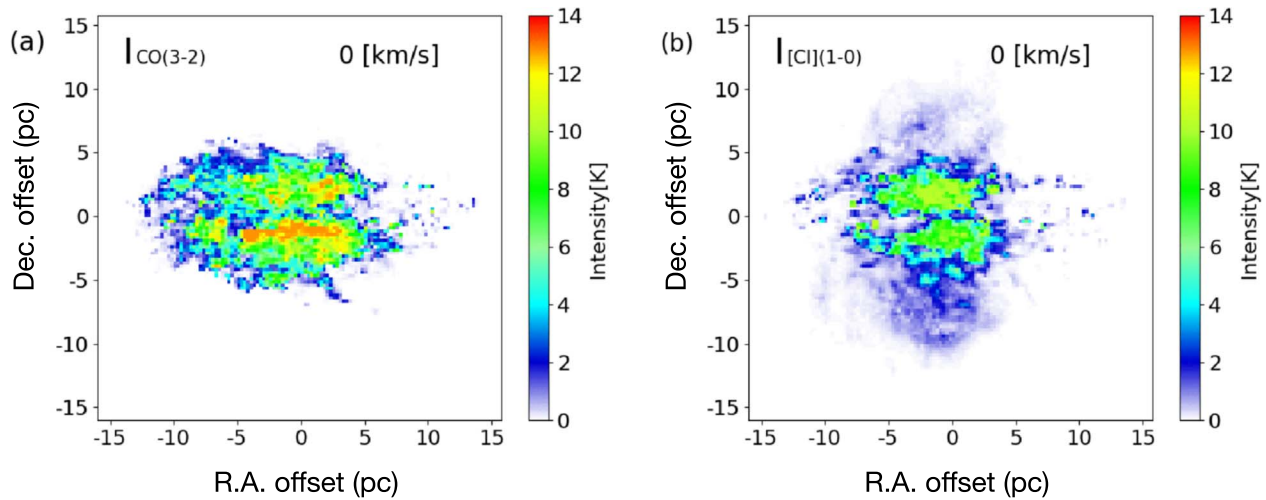


Figure 20. Simulated channel map of (a) CO(3–2) and (b) [C I](1–0) intensities (in units of brightness temperature) of the CND of the Circinus galaxy, with $i = 75^\circ$. Examples at the systemic velocity are shown. In both (a) and (b), the bulk of the emission stems from the region delineated by the CO(3–2), which corresponds to the geometrically thin mid-plane of the disk if viewed at $i = 90^\circ$ (i.e., an inclined thin disk; Figure 19). On the other hand, the spatially extended (or elongated along the vertical direction) component is only visible in the case of the [C I](1–0), as expected from Figure 19. This geometrically thick structure is due to the AGN-driven outflows.

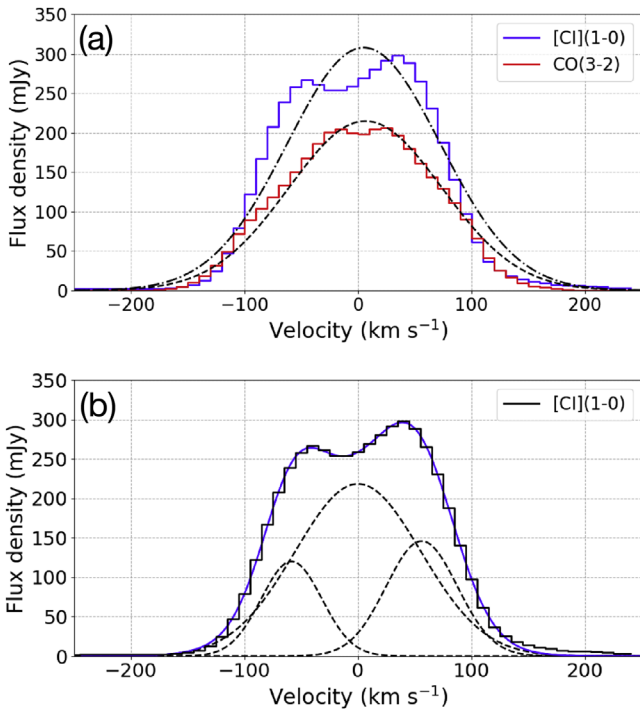


Figure 21. (a) Simulated line profiles of the [C I](1–0) and the CO(3–2) emission measured over the entire CND (see also Figure 19), seen with $i = 75^\circ$. The CO(3–2) follows a single Gaussian profile well (dashed line), while deviation from a single Gaussian profile (dotted–dashed line) is recognized in the case of the [C I](1–0). (b) The same [C I](1–0) spectrum as in (a), with a triple Gaussian fit line (each component is indicated by the dashed lines). The blueshifted and redshifted components represent the coherent outflows. The results of these fits are summarized in Table 7.

components are somewhat different from, the observed ones (see Tables 6 and 7). These discrepancies can be reconciled by adjusting some input parameters of the model (e.g., AGN luminosity, M_{H_2}), which are generally associated with considerable uncertainties. Lastly, we found that the outflow velocities of the [C I](1–0) implied by our observations (~ 60 and $\sim 75 \text{ km s}^{-1}$; Figure 18) will not significantly exceed the

Table 7
Results of the Gaussian Fit to the Model Spectra

	Peak (mJy beam $^{-1}$)	Centroid (km s $^{-1}$)	FWHM (km s $^{-1}$)
Single Gaussian			
CO(3–2)	214.7 ± 4.1	6.5 ± 1.0	158.6 ± 2.3
[C I](1–0)	307.8 ± 8.7	5.1 ± 2.2	158.3 ± 5.2
Triple Gaussians to the [C I](1–0) line			
Central	218.4 ± 0.4	0^a	130.7 ± 0.1
Blueshifted	120.0 ± 0.3	-58.5 ± 0.1	62.9 ± 0.1
Redshifted	145.9 ± 0.3	56.2 ± 0.1	74.0 ± 0.1

Note. The centroid velocities are measured with respect to the systemic velocity.

^a The centroid of this component was fixed to be 0 km s^{-1} for simplicity.

escape velocity (v_{esc}) from the vicinity of this AGN.¹⁵ Thus, a significant fraction of the gas carried by those winds will eventually fall back to the disk as failed winds. Therefore, given these consistencies, we conclude that our results support the view that a radiation-driven fountain including outflows indeed functions in the central region of Circinus to form a geometrically thick structure, which would explain the physical origin of its torus.

7. Summary

Our high-resolution ALMA observations of the CO(3–2) ($5.9 \text{ pc} \times 4.9 \text{ pc}$ resolution) and the [C I](1–0) ($14.5 \text{ pc} \times 13.4 \text{ pc}$ resolution) emission lines toward the CND of the Circinus galaxy revealed a wealth of detail about the atomic/molecular torus. In particular, we compared the observed results with predictions based on our multiphase dynamic torus model, where the

¹⁵ Even if we only consider the gravitational potential induced by the central SMBH, we will obtain high escape velocities of $v_{\text{esc}} = 120 \text{ km s}^{-1}$ at $r = 1 \text{ pc}$ and 70 km s^{-1} at $r = 3 \text{ pc}$, for example. Moreover, if we indeed use the V_{rot} found at the innermost few parsec region in this work ($\sim 70 \text{ km s}^{-1}$; Figure 16), we will also obtain a rather high v_{esc} of $\sim 100 \text{ km s}^{-1}$.

circulation of outflows, failed winds, and inflows of multiphase gas jointly and virtually constitute a geometrically thick structure that can replace the classic torus. The main findings of this work are summarized as follows:

1. Both Band 7 (351 GHz) and 8 (492 GHz) continuum emission were detected at the CND and spiral arms in the central 200 pc region of Circinus; these trace thermal dust emission. The CND appears as the inner extension of the larger-scale spiral arms and traces the region radially farther than the warm dust distribution seen in the $K_s/F814$ flux ratio map. This manifests the existence of a temperature-dependent circumnuclear dust structures.
2. The double Gaussian fit to the Band 7 continuum visibility data suggested a compact polar elongation at this submillimeter wavelength, in addition to a bright part of the extended CND. The size and orientation of the submillimeter polar elongation are consistent with those seen at MIR wavelengths, which challenges the classic torus paradigm.
3. The CND traced by both the CO(3–2) line (74 ± 3 pc \times 34 ± 1 pc, PA = 212°) and the [C I](1–0) line emission carries a huge amount of H₂ gas of $\simeq 3 \times 10^6 M_\odot$, with a beam-averaged column density of $N_{\text{H}_2} \simeq 5 \times 10^{23}$ cm^{–2}. This would contribute significantly to the Compton thickness of this AGN once beam dilution is corrected for, i.e., the CND plays an important role as a part of a nuclear obscurer or a torus.
4. We found an increasing trend for the [C I](1–0)/CO(3–2) line ratio in positions closer to the AGN. The ratio at the AGN position (brightness temperature scale; 14.5 pc \times 13.4 pc aperture) is ~ 0.9 , which is significantly higher than those observed in nearby starburst galaxies, for example. One possible explanation would be the XDR chemistry, where the AGN radiation efficiently dissociates CO molecules.
5. We decomposed the velocity fields traced by the CO(3–2) and the [C I](1–0) emission lines into intrinsic rotational velocities (V_{rot}) and dispersions (σ_{disp}) with tilted rings. The $\sigma_{\text{disp}}/V_{\text{rot}}$ profile (an indicator of the disk aspect ratio) based on the full-resolution CO(3–2) cube suggests that the dense molecular gas disk is geometrically thin (ratio ~ 0.25) at $r \gtrsim 15$ pc, whereas the ratio increases to ~ 0.4 at $r \lesssim 10$ pc. Within the qualitative framework of our model, the latter moderate thickness of the molecular disk at this spatial scale is consistent with a view that the material is puffed up due to the turbulence induced by the AGN-driven failed winds.
6. We found a possible indication of nuclear Keplerian rotational motion in the full-resolution CO(3–2) data. As the associated uncertainties are large, however, higher-

resolution observations are mandatory to make a firmer conclusion.

7. The $\sigma_{\text{disp}}/V_{\text{rot}}$ ratio of the [C I](1–0) velocity field at $r \lesssim 10$ pc is significantly higher than that probed by the CO(3–2) line (the uv range and the beam sizes are matched). This indicates that the diffuse atomic gas is extended in a geometrically thicker structure than the dense molecular gas, i.e., the torus has a multiphase dynamic structure. According to our model, outflows preferentially seen at ionized and atomic gas are the prime driver of this geometrically thick atomic disk at the nuclear scale.
8. We simulated detailed CO(3–2) and [C I](1–0) distributions and their line properties based on our multiphase dynamic torus model. We showed that the [C I](1–0) emission is indeed spatially more extended along the vertical direction of the disk than the CO(3–2) emission. The simulated [C I](1–0) line shows a deviation from a single Gaussian profile due to nuclear outflows, which is indeed consistent with the observed [C I](1–0) spectrum. The modest outflow velocity indicates that a significant fraction of the wind mass will fall back to the disk, i.e., failed winds, as expected in our model to function the fountain process.

Given various consistencies between the observations and our model predictions, we support the validity of the radiation-driven fountain scheme at the central region of Circinus, which would explain the longstanding mystery of the physical origin of the AGN torus.

We acknowledge the anonymous referee for his/her thorough reading and very constructive suggestions, which improved this paper significantly. We thank Dr. M. Mezcuta for kindly providing us the NIR K_s -band and *HST*/F814 data. This paper makes use of the following ALMA data: ADS/JAO.ALMA#2016.1.01613.S. ALMA is a partnership of ESO (representing its member states), NSF (USA), and NINS (Japan), together with NRC (Canada), NSC and ASIAA (Taiwan), and KASI (Republic of Korea), in cooperation with the Republic of Chile. The Joint ALMA Observatory is operated by ESO, AUI/NRAO and NAOJ. This work is supported by JSPS KAKENHI Grant Number 17K14247 (T.I.), 16H03959 (K.W.), and the JSPS Grant-in-Aid for Scientific Research (S) JP17H06130 (K.K.).

Appendix

Velocity channel maps of the CO(3–2) and [C I](1–0) emission lines are shown in Figures 22 and 23, respectively. These exhibit the circumnuclear spatial structures, including the CND and the three spiral arms (see also Figures 6 and 13).

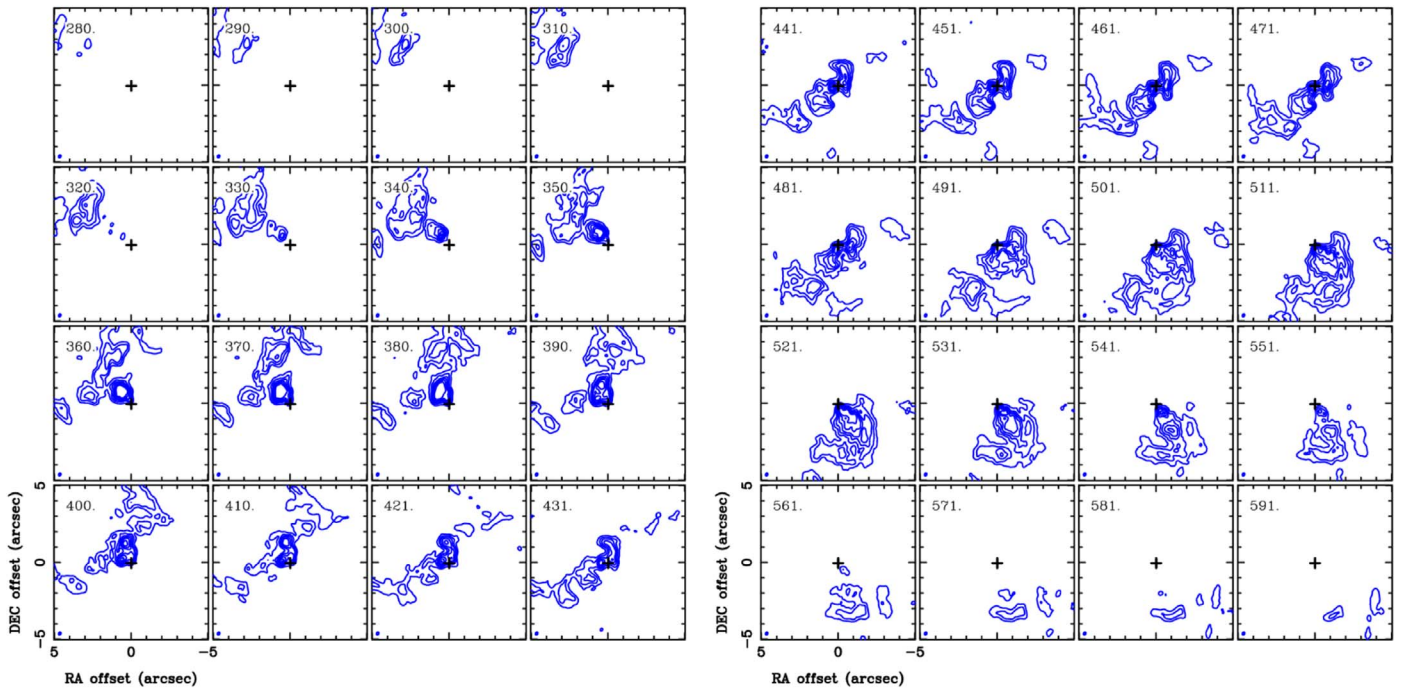


Figure 22. Velocity channel maps of the CO(3–2) emission line in the central $10'' \times 10''$ (or $\sim 200 \times 200 \text{ pc}^2$) box of the Circinus galaxy. The AGN position is indicated by the black plus sign. The velocity step is 10 km s^{-1} , and the central velocity of each channel is plotted in the upper left corner. Only bright emission are shown here (100, 200, 300, 400, 500, and 600σ ; $1\sigma = 0.37 \text{ mJy beam}^{-1}$), and negative contours are not shown, to enhance the clarity of the structure. Note that the synthesized beam size in these maps is $0''.29 \times 0''.24$ with $\text{PA} = 153^\circ.6$.

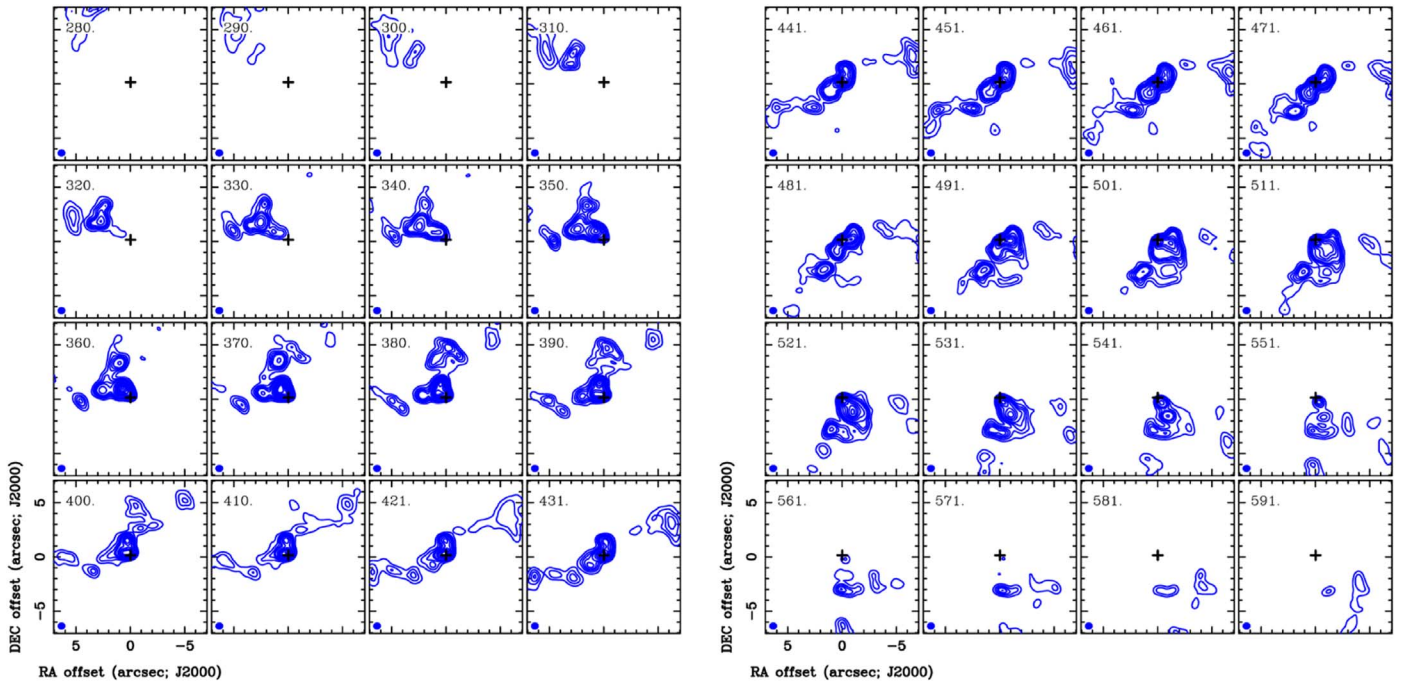


Figure 23. Velocity channel maps of the [C I](1–0) emission line in the central $10'' \times 10''$ (or $\sim 200 \times 200 \text{ pc}^2$) box of the Circinus galaxy. The AGN position is indicated by the black plus sign. The velocity step is 10 km s^{-1} , and the central velocity of each channel is plotted in the upper left corner. Only bright emission are shown here (20, 40, 60, 80, 100, 150, 200, 250, 300, 350, 400 and 450σ ; $1\sigma = 3.1 \text{ mJy beam}^{-1}$), and negative contours are not shown, to enhance the clarity of the structure. Note that the synthesized beam size in these maps is $0''.71 \times 0''.66$ with $\text{PA} = 95^\circ.9$.

ORCID iDs

Takuma Izumi  <https://orcid.org/0000-0001-9452-0813>
 Keiichi Wada  <https://orcid.org/0000-0002-8779-8486>
 Kotaro Kohno  <https://orcid.org/0000-0002-4052-2394>

References

Aalto, S., Johansson, L. E. B., Booth, R. S., & Black, J. H. 1991, *A&A*, 249, 323
 Aalto, S., Muller, S., Costagliola, F., et al. 2017, *A&A*, 608, 22

- Alonso-Herrero, A., Pereira-Santaella, M., García-Burillo, S., et al. 2018, *ApJ*, **859**, 144
- Antonucci, R. 1993, *ARA&A*, **31**, 473
- Arévalo, P., Bauer, F. E., Puccetti, S., et al. 2014, *ApJ*, **791**, 81
- Asmus, D., Hönig, S. F., Gandhi, P., et al. 2014, *MNRAS*, **439**, 1648
- Asmus, D., Hönig, S. F., Gandhi, P., et al. 2016, *ApJ*, **822**, 109
- Bayet, E., Gerin, M., Phillips, T. G., & Contursi, A. 2004, *A&A*, **427**, 45
- Bolatto, A. D., Wolfire, M., & Leroy, A. K. 2013, *ARA&A*, **51**, 207
- Burtscher, L., Meisenheimer, K., Tristram, K. R. W., et al. 2013, *A&A*, **558**, A149
- Casey, C. M., Narayanan, D., & Cooray, A. 2014, *PhR*, **541**, 45
- Clarke, C. J., Kinney, A. L., & Pringle, J. E. 1998, *ApJ*, **495**, 189
- Clemens, M. S., Negrello, M., De Zotti, G., et al. 2013, *MNRAS*, **433**, 695
- Curran, S. J., Johansson, L. E. B., Bergman, P., et al. 2001, *A&A*, **367**, 457
- Curran, S. J., Johansson, L. E. B., Rydbeck, G., & Booth, R. S. 1998, *A&A*, **338**, 863
- Curran, S. J., Koribalski, B. S., & Bains, I. 2008, *MNRAS*, **389**, 63
- Curran, S. J., Rydbeck, G., Johansson, L. E. B., & Booth, R. S. 1999, *A&A*, **344**, 767
- Davies, R. I., Müller Sánchez, F., Genzel, R., et al. 2007, *ApJ*, **671**, 1388
- de Vaucouleurs, G., de Vaucouleurs, A., & Corwin, Jr 1991, Third Reference Catalogue of Bright Galaxies. Vol. III, Data for Galaxies Between 12^h and 24^h (New York: Springer)
- Di Teodoro, E. M., & Fraternali, F. 2015, *MNRAS*, **451**, 3021
- Downes, D., & Solomon, P. M. 1998, *ApJ*, **507**, 615
- Draine, B. T. 2011, *Physics of the Interstellar and Intergalactic Medium* (Princeton, NJ: Princeton Univ. Press)
- Elitzur, M., & Ho, L. C. 2009, *ApJL*, **701**, L91
- Elitzur, M., & Shlosman, I. 2006, *ApJL*, **648**, L101
- Elmouttie, M., Haynes, R. F., Jones, K. L., et al. 1998a, *MNRAS*, **297**, 1202
- Elmouttie, M., Krause, M., Haynes, R. F., & Jones, K. L. 1998b, *MNRAS*, **300**, 1119
- Espada, D., Matsushita, S., Miura, R. E., et al. 2017, *ApJ*, **843**, 136
- Esquej, P., Alonso-Herrero, A., González-Martín, O., et al. 2014, *ApJ*, **780**, 86
- Freeman, K. C., Karlsson, B., Lynga, G., et al. 1977, *A&A*, **55**, 445
- Gallimore, J. F., Elitzur, M., Maiolino, R., et al. 2016, *ApJL*, **829**, L7
- García-Burillo, S., Combes, F., Ramos Almeida, C., et al. 2016, *ApJL*, **823**, L12
- Glover, S. C. O., Clark, P. C., Micic, M., & Molina, F. 2015, *MNRAS*, **448**, 1607
- Granato, G. L., & Danese, L. 1994, *MNRAS*, **268**, 235
- Greenhill, L. J., Booth, R. S., Ellingsen, S. P., et al. 2003, *ApJ*, **590**, 162
- Greenhill, L. J., Ellingsen, S. P., Norris, R. P., et al. 1997, *ApJL*, **474**, L103
- Guainazzi, M., Matt, G., Antonelli, L. A., et al. 1999, *MNRAS*, **310**, 10
- Hagiwara, Y., Miyoshi, M., Doi, A., & Horiuchi, S. 2013, *ApJ*, **768**, 38
- Harnett, J. I., Whiteoak, J. B., Gardner, F. F., et al. 1990, *MNRAS*, **244**, 130
- Hitschfeld, M., Aravena, M., Kramer, C., et al. 2008, *A&A*, **479**, 75
- Hollenbach, D. J., & Tielens, A. G. G. M. 1999, *RvMP*, **71**, 173
- Hönig, S. F., Beckert, T., Ohnaka, K., & Weigelt, G. 2006, *A&A*, **452**, 459
- Ikeda, M., Maezawa, H., Ito, T., et al. 1999, *ApJL*, **527**, L59
- Ikeda, M., Oka, T., Tatematsu, K., et al. 2002, *ApJS*, **139**, 467
- Imanishi, M., Nakanishi, K., & Izumi, T. 2016, *ApJL*, **822**, L10
- Imanishi, M., Nakanishi, K., & Izumi, T. 2018, *ApJL*, **853**, L25
- Imanishi, M., & Wada, K. 2004, *ApJ*, **617**, 214
- Israel, F. P. 1992, *A&A*, **265**, 487
- Israel, F. P., & Baas, F. 2001, *A&A*, **371**, 433
- Israel, F. P., & Baas, F. 2003, *A&A*, **404**, 495
- Israel, F. P., Rosenberg, M. J. F., & van der Werf, P. 2015, *A&A*, **578**, A95
- Israel, F. P., Tilanus, R. P. J., & Baas, F. 2006, *A&A*, **445**, 907
- Izumi, T., Kawakatu, N., & Kohno, K. 2016, *ApJ*, **827**, 81
- Izumi, T., Kohno, K., Fathi, K., et al. 2017, *ApJL*, **845**, L5
- Izumi, T., Kohno, K., Martín, S., et al. 2013, *PASJ*, **65**, 100
- Jaffe, W., Meisenheimer, K., Röttgering, H. J. A., et al. 2004, *Natur*, **429**, 47
- Jones, K. L., Koribalski, B. S., Elmouttie, M., & Haynes, R. F. 1999, *MNRAS*, **302**, 649
- Kaufman, M. J., Wolfire, M. G., Hollenbach, D. J., & Luhman, M. L. 1999, *ApJ*, **527**, 795
- Krieps, M., Martín, S., Sakamoto, K., et al. 2016, *A&A*, **592**, L3
- López-Gonzaga, N., Burtscher, L., Tristram, K. R. W., et al. 2016, *A&A*, **591**, A47
- Maiolino, R., Alonso-Herrero, A., Anders, S., et al. 2000, *ApJ*, **531**, 219
- Maloney, P. R., Hollenbach, D. J., & Tielens, A. G. G. M. 1996, *ApJ*, **466**, 561
- Marconi, A., Moorwood, A. F. M., Origlia, L., & Oliva, E. 1994, *Msngr*, **78**, 20
- Martí-Vidal, I., Vlemmings, W. H. T., Müller, S., et al. 2014, *A&A*, **563**, A136
- Matt, G., Fiore, F., Perola, G. C., et al. 1996, *MNRAS*, **281**, L69
- Matt, G., Guainazzi, M., Maiolino, R., et al. 1999, *A&A*, **341**, L39
- McMullin, J. P., Waters, B., Schiebel, D., et al. 2007, in *ASP Conf. Ser.* 376, *Astronomical Data Analysis Software and Systems XVI*, ed. R. A. Shaw, F. Hill, & D. J. Bell (San Francisco, CA: ASP), 127
- Meijerink, R., & Spaans, M. 2005, *A&A*, **436**, 397
- Mezcua, M., Prieto, M. A., Fernández-Ontiveros, J. A., & Tristram, K. R. W. 2016, *MNRAS*, **457**, L94
- Miyamoto, Y., Seta, M., Nakai, N., et al. 2018, *PASJ*, **70**, L1
- Moorwood, A. F. M., & Glass, I. S. 1984, *A&A*, **135**, 281
- Moorwood, A. F. M., Lutz, D., Oliva, E., et al. 1996, *A&A*, **315**, L109
- Müller Sánchez, F., Davies, R. I., Eisenhauer, F., et al. 2006, *A&A*, **454**, 481
- Murphy, T., Sadler, E. M., Ekers, R. D., et al. 2010, *MNRAS*, **402**, 2403
- Nagar, N. M., & Wilson, A. S. 1999, *ApJ*, **516**, 97
- Neškova, M., Ivezić, Ž., & Elitzur, M. 2002, *ApJL*, **570**, 9
- Neškova, M., Sirocky, M. M., Ivezić, Ž., & Elitzur, M. 2008a, *ApJ*, **685**, 147
- Neškova, M., Sirocky, M. M., Nikutta, R., et al. 2008b, *ApJ*, **685**, 160
- Ojha, R., Stark, A. A., Hsieh, H. H., et al. 2001, *ApJ*, **548**, 253
- Oka, T., Kamegai, K., Hayashida, M., et al. 2005, *ApJ*, **623**, 889
- Oliva, E., Marconi, A., Cimatti, A., & di Serego Alighieri, S. 1998, *A&A*, **329**, L21
- Oliva, E., Salvati, M., Moorwood, A. F. M., & Marconi, A. 1994, *A&A*, **288**, 457
- Pier, E. A., & Krolik, J. H. 1992, *ApJ*, **401**, 99
- Pier, E. A., & Krolik, J. H. 1993, *ApJ*, **418**, 673
- Plume, R., Bensch, F., Howe, J. E., et al. 2000, *ApJL*, **539**, 133
- Sault, R. J., Teuben, P. J., & Wright, M. C. H. 1995, in *ASP Conf. Ser.* 77, *Astronomical Data Analysis Software and Systems IV*, ed. R. A. Shaw, H. E. Payne, & J. J. E. Hayes (San Francisco, CA: ASP), 433
- Schartmann, M., Meisenheimer, K., Camenzind, M., et al. 2005, *A&A*, **437**, 861
- Schartmann, M., Meisenheimer, K., Camenzind, M., et al. 2008, *A&A*, **482**, 67
- Schartmann, M., Wada, K., Prieto, M. A., et al. 2014, *MNRAS*, **445**, 3878
- Schinnerer, E., Meidt, S. E., Pety, J., et al. 2013, *ApJ*, **779**, 42
- Shimajiri, Y., Sakai, T., Tsukagoshi, T., et al. 2013, *ApJL*, **774**, L20
- Solomon, P. M., & Vanden Bout, P. A. 2005, *ARA&A*, **43**, 677
- Solomon, P. M., Asmus, D., & Tristram, K. R. W. 2017, *MNRAS*, **472**, 3854
- Stalewski, M., Fritz, J., Baes, M., et al. 2012, *MNRAS*, **420**, 2756
- Suzuki, H., Yamamoto, S., Ohishi, M., et al. 1992, *ApJ*, **392**, 551
- Tristram, K. R. W., Burtscher, L., Jaffe, W., et al. 2014, *A&A*, **563**, A82
- Tristram, K. R. W., Meisenheimer, K., Jaffe, W., et al. 2007, *A&A*, **474**, 837
- Tully, R. B., Rizzi, L., Shaya, E. J., et al. 2009, *AJ*, **138**, 323
- Urry, C. M., & Padovani, P. 1995, *PASP*, **107**, 803
- Veilleux, S., & Bland-Hawthorn, J. 1997, *ApJL*, **479**, L105
- Viti, S., García-Burillo, S., Fuente, A., et al. 2014, *A&A*, **570**, 28
- Wada, K. 2012, *ApJ*, **758**, 66
- Wada, K. 2015, *ApJ*, **812**, 82
- Wada, K., Fukushige, R., Izumi, T., & Tomisaka, K. 2018, *ApJ*, **852**, 88, (Paper 1)
- Wada, K., & Norman, C. A. 2002, *ApJL*, **566**, L21
- Wada, K., Papadopoulos, P. P., & Spaans, M. 2009, *ApJ*, **702**, 63
- Wada, K., Schartmann, M., & Meijerink, R. 2016, *ApJL*, **828**, L19
- Walter, F., Weiß, A., Downes, D., et al. 2011, *ApJ*, **730**, 18
- Weiß, A., Downes, D., Henkel, C., & Walter, F. 2005, *A&A*, **429**, L25
- Wilson, A. S., Shopbell, P. L., Simpson, C., et al. 2000, *AJ*, **120**, 1325
- Zhang, Z.-Y., Henkel, C., Gao, Y., et al. 2014, *A&A*, **568**, 122
- Zschaechner, L. K., Walter, F., Bolatto, A., et al. 2016, *ApJ*, **832**, 142